Raman Spectroscopy Study of Manganese Oxides – Layer Structures **Revision 1**

Jeffrey E. Post[1], David McKeown[2], Peter J. Heaney[3]

[1]Department of Mineral Sciences, National Museum of Natural History, Smithsonian Institution, Washington, DC, 20013-7012, USA; [2]Vitreous State Laboratory, The Catholic University of America, Washington, DC 20064, USA; [3]Department of Geosciences, Penn State University, 540 Deike Building, University Park, PA 16802, USA

*Corresponding author: Jeffrey Post, postj@si.edu

Abstract

Raman spectra were collected for an extensive set of well-characterized layer-structure Mn oxide mineral species (phyllomanganates) employing a range of data collection conditions. We show that the application of a variety of laser wavelengths, such as 785, 633, and 532 nm, at low power levels (30 – 500 μW) in conjunction with the comprehensive database of standard spectra presented here, makes it possible to distinguish and identify the various phyllomanganate minerals. The Raman mode relative intensities can vary significantly as a function of crystal orientation relative to the incident laser light polarization direction as well as incident laser light wavelength. Consequently, phase identification success is enhanced when using a standards database that includes multiple spectra collected for different crystal orientations and with different laser light wavelengths. The position of the highest frequency Raman mode near 630-665 cm^{-1} shows a strong linear correlation with the fraction of Mn^{3+} in the octahedral Mn sites. With the comprehensive Raman database of well-characterized Mn oxide standards provided here (and available online as supplemental materials), and use of appropriate data collection conditions, micro-Raman is a powerful tool for identification and characterization of biotic and abiotic Mn oxide phases from diverse natural settings, including on other planets, as well as for laboratory and industrial materials.

Keywords: Manganese Oxide, Raman Spectroscopy, Phyllomanganates, Birnessite

INTRODUCTION

Layer-structure Mn oxide minerals, also called phyllomanganates, are found in a wide variety of geological settings and are important constituents in many soils and sediments (Post, 1999). These phases can precipitate from solution as the result of macro or microscale changes in redox conditions, pH, or composition; additionally, natural and laboratory Mn oxides that form by biologically mediated processes are predominantly phyllomanganates (McKeown and Post 2001; Tebo et al. 2004; Santelli et al. 2011). Phyllomanganates having a birnessite-like structure readily participate in redox and cation-exchange reactions and exhibit high adsorption capacities for a variety of organic pollutants and toxic metallic ions (Le Goff et al. 1996; Manning et al. 2002; Feng et al. 2007; Lopano et al. 2009; Kwon et al. 2013; Fleeger et al. 2013; Shumlas et al., 2016; Kong et al. 2019). They also have been identified as promising heterogeneous compounds for water-oxidation catalysis (Sauer and Yachandra, 2002; Jiao and Frei, 2010; Wiechen et al., 2012; Frey et al.; 2014; Feng et al., 2017). Phyllomanganates are critical battery materials and are being investigated for their applications as catalysts and cation-exchange agents, as well as for their potential to mitigate hazardous materials in the environment (Ghodbane et al. 2009; Li et al. 2012; Nam et al. 2015).

Phyllomanganates are constructed of sheets of MnO_6 octahedra. The Mn is predominantly Mn^{4+} but can be substituted by Mn^{3+} and vacancies, with the resulting layer charges being compensated by various interlayer cations in the different phases (Fig. 1). Most phyllomanganates also have interlayer water molecules. Natural samples commonly are fine-grained and poorly crystalline, and the particular phyllomanganate mineral phases are difficult to distinguish visually in the field or in hand specimens. They also can occur as fine-scale intergrowths of two or more phases that readily alter from one to another. In many cases, X-ray diffraction (XRD) of these phases also fails to identify them, since the XRD patterns often exhibit broad peaks from multiple disordered phases, making basic phase identification difficult or impossible (Ling et al. 2020). Consequently, many researchers employ other methods in addition to XRD to characterize natural phyllomanganates, such as X-ray absorption spectroscopy (XAS), Fourier transform infrared spectroscopy (FTIR), transmission electron microscopy (TEM), and combined energy-dispersive X-ray spectroscopy and scanning electron microscopy (EDS-SEM). These techniques also have experimental limitations and requirements, such as special sample preparation methods, large sample sizes, or synchrotron X-ray sources.

Due to the difficulties of working with complex and typically poorly crystalline natural phyllomanganate samples, many researchers use synthetic phases that are presumed to be suitable analogs of the minerals. Offsetting the advantages of working with pure, relatively well-crystalline laboratory-produced samples is the difficulty of assessing their relevancy to natural phases or systems. Additionally, complexities and confusion introduced using multiple synthesis methods, and terminology, can cause problems comparing results among different research groups.

In a recent paper, we demonstrated the advantages of using micro-Raman spectroscopy to routinely identify and characterize tunnel-structure Mn oxide phases for a variety of natural and synthetic samples (Post et al. 2020). Here we extend that work to the phyllomanganates. During the past few decades, numerous reports have described applications of Raman spectroscopy to Mn oxides, primarily as an identification tool, but also for investigating changes in response to certain redox, cation-exchange, and other reactions (Bernard et al. 1993). There are several studies that have used Raman spectroscopy to study phyllomanganates (e.g. Bernard et al. 1993; Kim and Stair 2004; Julien et al. 2003; Julien et al. 2004; Hsu et al. 2011; Burlet and Vanbrabant

2015; Yang et al. 2019; Boumaiza et al. 2019; and Bernardini et al. 2019) with various degrees of success. Such work has been invigorated in part by advancements in micro-Raman techniques that have resulted in greater availability of in-house Raman systems. Modern systems typically offer multiple laser options with high-sensitivity detectors that provide a range of data collection conditions that can be optimized for particular samples. Additionally, Raman spectrometers fitted with high quality microscopes permit rapid *in situ* interrogation of samples with spatial resolution approaching one micron or less. Micro-Raman systems have the potential to provide phase identification and structural information quickly and easily from discrete areas on natural or synthetic Mn oxide samples. In particular, the combination of Raman microscopy and analytical SEM provides unparalleled insights into the micro-mineralogy and -chemistry of complex samples.

Our study of the tunnel structure Mn oxides (Post et al. 2020) confirmed the importance of using low laser powers (e.g. < 0.35 mW) and multiple laser wavelengths (e.g. 532, 633, and 785 nm) in order to obtain the most useful Raman spectra for phase identification and for elucidating structure information. These considerations are critical for the large tunnel-structure Mn oxides, such as todorokite and romanechite, but are equally so for the phyllomanganates, and in particular, for the birnessite-like phases that are important in many natural systems.

In the work presented here, we provide results from the most comprehensive-to-date Raman spectroscopy study of layer-structure Mn oxide phases. Raman spectra were collected from a large number and variety of natural and synthetic samples, drawing from the Smithsonian Institution mineral collection, and additional samples from various sources, which had been characterized in detail as part of our long-term research program on Mn oxides. Raman spectra were collected using multiple Raman systems with a range of laser wavelengths in order to provide comparisons and to determine optimal data collection conditions. Additionally, we present representative spectra from different specimens, localities, and crystal orientations. A major goal of this study is to provide a spectral database for identifying the various layer-structure Mn oxide mineral phases, with an emphasis on natural samples. Finally, we explore spectral trends and details for some specific phases that provide insights about composition, symmetry, and in some circumstances, Mn oxidation states.

EXPERIMENTAL METHODS

Specimens

The layer-structure Mn oxide mineral samples for which spectra are presented here are listed in Table 1, including information about individual compositions. Structure symmetry and factor group analyses (Fateley et al. 1972) for the various phases are presented in Table 2. A variety of samples were included to represent variations in composition, structural disorder, and locality. All samples were checked by powder X-ray diffraction (XRD) to confirm phase identification and purity. Energy-dispersive X-ray spectroscopy (EDS) analyses and backscattered electron imaging were used to determine composition and assess chemical homogeneity. Where possible, single crystals, or crystal fragments, were selected for Raman measurements; fine-grained samples were lightly crushed, or in some cases, prepared as polished sections that were also used for chemical analyses. For some Raman measurements, loose sample grains were placed on glass slides without adhesive, which can introduce strong luminescence. The synthetic triclinic Na-birnessites included the same material studied by Post and Veblen (1990) as well as samples more recently synthesized and described in Ling et al. (2018). Synthetic birnessites with different compositions were prepared by cation-exchange, following the procedure of Golden et al. (1986). The hexagonal birnessite samples were prepared by reacting Na-birnessite with a pH 2 HCl solution.

X-ray diffraction (XRD)

Samples were characterized by powder XRD using a Rigaku II D/MAX-RAPID micro-diffractometer (Department of Mineral Sciences, Smithsonian Institution) equipped with a graphite monochromator and a curved image plate area detector. A Mo tube (50 kV, 40 mA) was used as the X-ray source with a 0.3 mm collimator. Small (~1 mm) balls of powdered samples (with added super-glue as needed), or fragments of fine-grained polycrystalline materials, were mounted on tips of glass fibers. During exposure to X-rays, the sample was rotated at 1°/min on phi to minimize the effects of sample heterogeneity and preferred orientation. The full set of Debye-Scherrer diffraction rings from the imaging plate data were integrated using Rigaku-provided software, and interpretation of XRD patterns was performed using the JADE 9 software package. Phase identifications were confirmed using the ICDD PDF-4 Minerals database and an in-house collection of well-characterized Mn oxide mineral standards. Representative XRD patterns are deposited as supplementary data with *American Mineralogist*.

Scanning electron microscopy

Uncoated samples (which then could also be used for Raman analysis) were mounted on carbon tape adhered to an aluminum stub and analyzed with scanning electron microscopy (SEM) using a field emission source (FEI Apreo) equipped with an EDAX Octane Silicon Drift EDS detector (Department of Mineral Sciences, Smithsonian Institution). Backscattered electron (BSE) images were collected, and EDS analysis was used to determine the chemical composition and homogeneity of the Mn oxide samples (with beam current of 1.6 nA). The images were collected and analyses performed in low vacuum (0.31 torr) at an accelerating voltage of 15 kV. The data were processed using the Noran System Six 3 (NSS 3) software.

Raman spectroscopy

The reproducibility of the Raman spectra and the optimal data collection conditions were evaluated by using four different micro-Raman systems at 25 °C in back-scattering geometry using a single-grating spectrograph with notch filters. Two HORIBA LabRam HR Evolution systems were employed (Department of Mineral Sciences, Smithsonian Institution; and Materials Characterization Laboratory, Penn State University), both equipped with Synapse back-illuminated deep depleted, Peltier cooled 1024 x 128 element CCD cameras. The spectra presented in this paper were collected using 532, 633 (Penn State), and 785 nm solid state lasers with 300 and 600 gr/mm spectrograph gratings, respectively, for spectral resolutions near 4 cm^{-1}. An Olympus 100x or 50x objective was used to focus the incident laser light onto the sample. The characteristic 520 cm^{-1} line from a Si wafer standard was used for Raman frequency calibration. The laser power at the sample was measured using a Thorlabs power meter (PM100USB) for the various combinations of microscope objectives and lasers. Typically, spectra were collected using laser powers of 540 μW or less for the 532 nm laser and 350 μW or less for the 633 and 785 nm lasers. Some phases, e.g. chalcophanite and lithiophorite, did not exhibit obvious spectral changes at laser powers up to 2 mW, but birnessite-like phases showed evidence of sample degradation or phase transformation at laser powers above ~500 μW at the sample. For the 532 nm laser, spectra for birnessite-like phases exhibited changes at powers as low as 30 μW. The laser power measurements are intensities of the focused incident laser beam at the sample, not power densities, which vary depending upon the laser spot size, determined by the objective used, laser focus, and certain other instrumental and sample surface characteristics.

The second system (Vitreous State Laboratory, Catholic University) consists of a WITec alpha-300 RA+ micro-Raman system, where 633 nm solid state diode and 532 nm DPSS lasers were used with a 600 gr/mm grating to disperse the Raman scattered light on to a 1024 x 128 element Peltier cooled CCD camera (Andor Technology Model DV401A-BVF-352). 50x and 100x Zeiss objectives were used producing a ~1 μm laser spot size on the sample. The spectra were frequency calibrated to the Si 520 cm^{-1} mode. The spectral resolution of the data produced from these system configurations is near 6 cm^{-1}. Spectra for birnessite-like phases showed phase alteration at powers as low as 150 μW using 633 nm laser light.

A third system (Vitreous State Laboratory, Catholic University) consists of a Melles-Griot Model 45 Ar^+ laser that provided 457.9 and 514.5 nm wavelength light that was guided through a long working distance Mitutoyo 10x microscope objective and focused to a 10 μm diameter spot on the sample. The scattered light proceeded through holographic notch and super-notch filters (Kaiser Optical Systems), which reduced the Rayleigh (or elastically) scattered light intensity by ten optical densities. The Horiba HR460 spectrograph used a 1200 gr/mm grating (Richardson Grating Laboratory) to disperse the Stokes scattered light from the sample on to a 2048 x 512 element Peltier cooled CCD detector (Andor Technology Model DU440BV). Due to the relatively broad spectral features for most samples measured, the spectrograph incident slits were set to 6 cm^{-1} spectral resolution. The spectrograph was frequency calibrated using CCl_4, such that recorded Raman mode frequencies for all spectra are accurate to within ±1 cm^{-1} of the actual values. The laser power for this system was minimized to <0.1 mW at the sample to avoid sample heating and alteration.

For each sample, initial data collection was performed using minimal laser power, e.g. 30 μW; the power level was gradually increased until noticeable changes occurred to the spectra, such as variations in peak intensities, the appearance of new peaks, or broad band luminescence with evidence of sample darkening or hole formation at the incident laser light position. Where possible, relatively flat and smooth sample surfaces, as ascertained at 100x or 50x magnification, were selected for data collection, using 5- to 60-second integration times per acquisition, with two to 10 acquisitions per spot to improve signal-to-noise levels in the spectra. Crystal orientation effects were apparent for most layer-structure Mn oxide phases. Phyllomanganate crystals typically have a platy morphology and tended to orient preferentially with the Mn octahedral sheets normal to the direction of the laser beam. When possible, spectra were collected with crystals oriented such that the octahedral sheets were both parallel and perpendicular to the direction of the incident laser light. Polarized spectra were gathered using an analyzer polarizer inserted in the scattered light path. Polarized spectra were labeled VV (vertical-vertical) or VH (vertical-horizontal) to describe collection conditions where the laser light polarization was oriented parallel or perpendicular, respectively, to the polarization direction of the analyzer. For comparison, unpolarized spectra also were collected without an analyzer in the scattered light path between the sample and spectrograph.

Lattice Dynamics Calculations

In order to provide guidance for some general vibrational assignments to the observed Raman features, preliminary normal coordinate valence-force lattice dynamics (LD) calculations at zero wavevector (Dowty 1987 and 2007) were performed for several of the phyllomanganate structures. The models included Mn-O stretch as well as O-Mn-O bend force constants to simulate the various bonding environments within the linked MnO_6 octahedra. Interlayer cation-oxygen stretch force constants were also included. The force constants were allowed to vary so that the calculated mode frequencies best matched the set of observed mode frequencies from the Raman spectra for each phase.

Overall, LD calculations indicated that Raman-active modes for these Mn-oxides can be divided into two frequency ranges. Consistent with previous interpretations by Julien et al. (2003, 2004), modes above 500 cm^{-1}, are dominated by MnO_6 octahedral deformations, including O-Mn-O bend, Mn-O stretch, as well as expansion and compression of the octahedra in the layer stacking direction, and shear motions of layers of O atoms that are parallel to the MnO_6 layers. In structures with higher symmetry Mn-sites, e.g. Mn on a symmetry center, the internal Mn octahedral modes involve O motions, while the Mn atoms are stationary. Modes at frequencies less than 500 cm^{-1} include contributions from displacements of interlayer cations, such as Zn^{2+} in chalcophanite and Na^+ in birnessite, and cation-water and water-water interactions.

RESULTS

Chalcophanite Group

Chalcophanite ($ZnMn_3O_7 \cdot 3H_2O$; Space Group *R*-3) is constructed of sheets of Mn^{4+}-O octahedra with one out of seven octahedra vacant. Single-crystal X-ray diffraction studies (Post and Appleman 1988) indicate that the vacancies are fully ordered within the octahedral sheets. Zn^{2+} cations sit above and below the vacancies and are in octahedral coordination with three O atoms from the octahedral sheet and three O atoms from the interlayer water molecules (Fig. 1). Jianshuiite and ernienickelite are isostructural with chalcophanite, but have Mg^{2+} and Ni^{2+}, respectively, as the dominant interlayer cations. Chalcophanite group minerals commonly occur as euhedral platy crystals.

Chalcophanite typically gives strong Raman features, especially for 532 and 633 nm laser light that are consistent for laser powers less than ~0.5 mW. Chalcophanite spectra are highly sensitive to laser light polarization, especially the Mn-O vibrational modes near 670 cm^{-1} that are intense in parallel polarized light but almost absent in the crossed polarized spectrum (Fig. 2). Similar polarization behavior for these modes is also observed for other phyllomanganates. By contrast, there are only small intensity differences for analogous peaks in crossed versus parallel polarized spectra for the large tunnel structure phases such as todorokite and romanechite (Post et al. 2020). Raman spectra for chalcophanite using 532, 633 and 785 nm lasers are similar (Fig. 3). The 670 cm^{-1} mode for chalcophanite has the greatest frequency of any of the layer Mn oxides, presumably because all the Mn is in the 4+ valence state, which imposes the shortest possible average Mn-O distance, and correspondingly the highest frequency vibrational motions. As discussed below, substitution of Mn^{4+} by the larger Mn^{3+}, with its attendant Jahn-Teller distortions, shifts the corresponding peaks to lower frequencies and increases the number of internal MnO_6 modes.

The Raman spectra for chalcophanite, jianshuiite, and ernienickelite are similar, but some variations, e.g. extra peaks near 533 and 590 cm^{-1}, suggest some fundamental differences in the Ni-bearing ernienickelite (Fig. 4). A detailed structure refinement has not been reported for ernienickelite. Spectra collected from chalcophanite with the laser light polarization direction parallel versus perpendicular to the octahedral sheets (Fig. 5a) show modest variations in intensities of several modes. Spectra collected with the laser polarization perpendicular to the layers for chalcophanite and ernienickelite show modes at ~3320 and 3390 cm^{-1} (Fig. 5b) that correspond to OH stretch vibrations from the interlayer water molecules; these modes were absent in spectra collected with the laser polarization parallel to the octahedral sheets, indicating that the predominant OH stretch motion is perpendicular to the sheets.

Lattice dynamic calculations for the chalcophanite structure (Figs. 6a and b) indicate that modes above ~500 cm^{-1} are due primarily to internal MnO_6 deformation, as well as expansion and compression of the MnO_6 layers. There are also Zn-O stretch contributions with Zn translating perpendicular to the octahedral layers, but as there are more MnO_6 octahedra than ZnO_6 octahedra, these modes are dominated by internal MnO_6 displacements. Modes below 500 cm^{-1} arise from mixtures of MnO_6 deformations and motions involving the interlayer Zn^{2+} cations and water molecules in ZnO_6 octahedra, where three of the coordinating oxygens are from water molecules. The Zn-H_2O stretch and the water motions become more dominant in the lower frequency modes. The lower frequency parallel polarized A_g modes arise from Zn translations perpendicular to the octahedral layers, while lower frequency crossed polarized B_g modes result primarily from Zn translations parallel to the octahedral layers. Not surprisingly, the most obvious differences among the spectra for chalcophanite compared with those for jianshuiite and ernienickelite are in this lower frequency region, presumably related to the different sizes and bonding properties of the Zn^{2+} versus Mg^{2+} and Ni^{2+} interlayer cations, respectively.

Granciéite Group

Granciéite, a Ca-rich phyllomanganate, has been found as an abiotic product in low-temperature alpine vein deposits and in oxidized zones of Fe and Mn deposits (Ertle et al. 2005). Recent studies, however, of naturally occurring phyllomanganates from fresh-water environments revealed Ca to be the predominant interlayer cation, sometimes associated with Mg, Ba, and/or K (Bargar et al. 2009; Tan et al. 2010; Ling et al. 2020). Furthermore, ranciéite-like structures play critical roles in water-oxidation catalysis and as the oxygen-evolving complex within the enzyme photosystem II (PSII) (Umena et al. 2011; Zhang et al. 2015; Yamaguchi et al. 2017).

Ranciéite has a hexagonal structure (*P*-3), and like chalcophanite consists of sheets of $Mn^{4+}O_6$ octahedra, but with one out of ten (or eleven) octahedra vacant, and Ca^{2+} and water molecules in the interlayer regions (Kim 1991, Post et al. 2008). X-ray diffraction and selected area electron diffraction patterns show no superstructure reflections, indicating that vacancies are not ordered in the octahedral sheets, presumably because of the relatively fewer vacancies, and therefore less energetic drive to order, compared with chalcophanite. The interlayer cations occupy sites above and below the octahedral vacancies and are predominately Ca^{2+} in ranciéite and Mn^{2+} in takanelite; other similar sized divalent cations, such as Ba^{2+}, Sr^{2+}, and Mg^{2+} are commonly found in ranciéite and takanelite specimens (Table 1 and Kim 1991). The interlayer cations are coordinated to three octahedral O atoms and three interlayer water O atoms. The interlayer-cation to Mn octahedral site ratio is ~0.2 (compared to 0.33 in chalcophanite), and the total interlayer cation charge is approximately +0.75. The larger sizes of the interlayer cations in ranciéite relative to those in chalcophanite group minerals might limit the numbers of cations that can fit into the interlayer region. The chemical analyses for the ranciéite samples used in this study, as well as Mn and interlayer cation occupancy factors determined by Rietveld refinements (Post et al. 2008), indicate that Mn^{2+} is absent or present in only minor amounts as an interlayer cation. The powder X-ray diffraction patterns and Raman spectra suggest that the ranciéite structure is like those of the synthetic Ca-birnessites generated when Na-birnessite is exchanged at low pH and low Ca concentrations (Elmi et al. 2020).

As with chalcophanite, the parallel and crossed polarized spectra of ranciéite (Fig. 7) reveal a strong polarization response, especially for the A_g internal MnO_6 modes near 667 and 578 cm^{-1}, which arise from mostly symmetric stretch vibrations that can only effectively scatter light polarized in the same direction as the incident laser beam; hence, these prominent high frequency features nearly disappear in the cross polarized spectrum. Unpolarized ranciéite spectra collected using 532, 633 and 785 nm laser wavelengths are plotted in Figure 8, and for several different ranciéite specimens in Figure 9. Not surprisingly, there is a resemblance between the chalcophanite and ranciéite spectra, but the ranciéite peaks generally are broader, presumably because of the lower crystal structure symmetry for ranciéite (*P*-3 vs. *R*-3), and the disordered vacancies in the octahedral sheets. Also, modes below 300 cm^{-1} are weaker or absent for ranciéite, relative to chalcophanite, likely resulting from interlayer cation disorder related to the random Mn site vacancies, and the variety of interlayer cations commonly found in natural samples. Powder XRD patterns for ranciéite samples typically exhibit broad diffraction peaks that also suggest structural disorder. The highest frequency Raman modes observed for various ranciéite specimens (near 667 cm^{-1}) are comparable to those seen in the chalcophanite spectra, suggesting that the Mn is tetravalent; this is consistent with Rietveld refinements (Post et al. 2008) showing ranciéite Mn-O bond distances comparable to those reported for chalcophanite (Post and Appleman 1988).

Ranciéite structure LD calculations (Fig. 10) include A_g modes at ~665 and 564 cm^{-1} dominated by expansion - compression motions of the MnO_6 octahedral sheets parallel to the *c*-axis, the layer stacking direction, with some Ca^{2+} translation parallel to the *c*-axis. Calculated E_g

modes at 621 and 396 cm^{-1} arise from MnO_6 octahedral shear within the layer. The lower frequency modes are dominated by interlayer water translations parallel (443 and 508 cm^{-1}) or perpendicular (363, 384, and 420 cm^{-1}) to the layer stacking direction. The calculations do not explain the observed A_g mode near 605 cm^{-1}, nor most observed modes below 400 cm^{-1} (Fig. 8) that may be due to motions of the interlayer cations (Ca^{2+}) near MnO_6 octahedra layer defects or water molecules.

Birnessite-like Phases

Birnessite was first described by Jones and Milne (1956) as a natural phase discovered in Aberdeenshire, Scotland with a chemical formula of $Na_{0.7}Ca_{0.3}Mn_7O_{14} \cdot 2.8{\cdot}H_2O$. Subsequently, numerous natural phases with “birnessite-like” structures have been described, including rancíéite (Post et al. 2008), takanelite (Nambu and Tanida 1971; Kim 1991), and lagalyite (Witzke et al. 2017). They commonly occur as fine-grained, poorly crystalline aggregates and coatings, making the studies of their structures and behaviors challenging. Additionally, various synthetic birnessite-like structures containing almost every possible alkali and alkaline earth element, as well as many of the transition metals, have been synthesized (*e.g.*, McKenzie, 1971; Golden et al., 1986) in attempts to elucidate the structural and chemical features of birnessite-like phyllomanganates (*e.g.*, Post and Veblen, 1990; Drits et al., 1997; Silvester et al., 1997; Lanson et al., 2000; Post et al., 2002; Feng et al., 2004; Händel et al., 2013) and their reactivities (*e.g.*, (Manceau et al., 2002; Feng et al., 2007; Lopano et al., 2007, 2011; Landrot et al., 2012; Wang et al., 2010; Kwon et al., 2013; Lefkowitz et al., 2013; Yin et al., 2013; Fischel et al., 2015; Hinkle et al., 2016; Zhao et al., 2016; Fischer et al. 2018). Laboratory studies have also demonstrated that formation of birnessite-like phases can be initiated, or enhanced, by certain microbes and fungi (Tebo et al. 2004; Webb et al. 2005; Grangeon et al. 2010; Santelli et al. 2011), and it is therefore likely that biologically mediated birnessite-like phyllomanganates are important in natural systems.

The birnessite structure is constructed of stacked layers of nominally $Mn^{4+}O_6$ octahedra; substitution of Mn^{3+} or other lower valence cations and vacancies for Mn results in a net negative charge on the octahedral sheets (Fig. 1). The charge is offset by addition of large mono- or divalent cations (e.g. Na^+, Ba^{2+}, K^+, Ca^{2+}) into the interlayer region, along with water molecules. Birnessite-like phases with predominantly Mn^{4+} exhibit overall hexagonal (trigonal) or near-hexagonal symmetry. As the proportion of Mn^{3+} increases, the associated Jahn-Teller distortions lower the symmetry to triclinic (Silvester et al. 1997; Ling et al. 2018). Birnessite-like structures exhibit a characteristic ~7 Å repeat in the layer stacking direction. In buserite phases, a double layer of water molecules between the octahedral sheets expands the layer spacing to ~10 Å.

Raman spectra collected using a 785 nm laser are shown for triclinic synthetic Na-birnessite and hexagonal-birnessite in Figure 11. The octahedral layers in Na-birnessite $[(Na^+_{0.29}, Mn^{2+}_{0.02,} H^+_{0.05}) (Mn^{3+}_{0.38}, Mn^{4+}_{0.62}) O_2 \cdot 0.75H_2O]$ (Post et al. 2002) have ~38% Mn^{3+} (Ilton et al 2016) and no vacancies. H-birnessite has ~20% Mn^{3+} (Ilton et al 2016), mostly in the interlayer region, and ~10% of the Mn octahedra are vacant (Ling et al 2018). The Raman spectra collected for Na-birnessite using 457.9, 633 and 785 nm lasers are plotted in Figure 12a. All spectra for birnessite-like phases collected using 532 nm laser light, even with power levels at 0.03 mW, show significant evidence of alteration due to laser heating, presumably related to the higher energy of the shorter wavelength light. Other observations suggest that 785 nm laser light consistently yields reproduceable spectra with no evidence of sample degradation for laser powers below about 0.3 mW. Spectra collected with 457.9 and 633 nm laser light at power levels near 0.1 mW are similar to those for 785 nm (Fig. 12a), with indications of sample alteration at powers as low as 0.15 mW (Fig. 12b).

LD calculations for Na-birnessite used a simplified higher symmetry *C*2/*m* monoclinic structure (the triclinic structure is close to having monoclinic symmetry), due to uncertainties arising from disorder among the H, Na, and O(w) positions. Similar to other phyllomanganates, LD calculations (Fig. 13) indicate that the highest frequency Raman peaks, e.g. the A_g mode at 640 cm^{-1} for Na-birnessite, arise primarily from MnO_6 octahedral expansion and compression motions parallel to the layer stacking direction. The next highest frequency modes, A_g and B_g at ~586 and 566 cm^{-1}, respectively, arise from shear motions of O atoms parallel to the MnO_6 layers. At frequencies below 500 cm^{-1}, calculated modes are dominated by translations of the interlayer Na and H_2O.

Raman spectra collected from synthetic birnessite-like phases having different interlayer cations are plotted in Figure 14. The spectra are similar at frequencies above 300 cm^{-1}, indicating that the MnO_6 octahedral sheets were not generally affected by the exchanges of the interlayer cations. A notable exception, however, involves the positions of the highest frequency peaks, ranging from 651 cm^{-1} for Ca-birnessite to 636 cm^{-1} for K-birnessite. As described below, these disparities likely reflect variations in Mn^{3+} concentration, which in turn depends on the valence charges and sizes of the interlayer cations. The most noticeable differences among the various birnessite spectra are in the lower frequency modes, which are governed by interlayer cation motions, as shown by our LD calculations. These modes are most intense for triclinic structures whose interlayer cations occupy positions at or near the midpoint between the MnO_6 layers, e.g. for Na^+-, K^+-, Li^+-, and Ba^{2+}-birnessites (Post and Veblen 1990; Lopano et al. 2007). In some cases, the Raman spectra might reveal the identity of the predominant interlayer cation and its site symmetry; for example, a strong peak near 97 cm^{-1} is present only for K-birnessite (Fig. 14). Also, compared with other compositions, K-exchanged birnessite typically showed sharper Raman peaks, suggesting that K^+ is particularly well accommodated by the birnessite structure.

Vernadite

Vernadite is a poorly crystalline natural Mn oxide phase characterized by a powder XRD pattern with broad peaks at 2.46, 1.42, and rarely at 2.2 Å. It was first described and named by Betekhtin (1940). Vernadite is commonly described as a birnessite that is turbostratically disordered in the layer stacking direction, or a birnessite with crystallites with so few MnO_6 layers that powder XRD patterns show no basal reflections (Buser et al. 1954; Bricker 1965; Giovanoli, 1980; Drits et al. 1997; Grangeon, 2012). Chukrov et al. (1987) concluded, however, that birnessite and vernadite are distinct. Chemical analyses of vernadite typically show minor amounts of K, Mg, Ca, Ba, and Fe with 15-25 wt.% water as compared with approximately 12 wt.% water in Na-birnessite (Chukrov et al. 1978). Vernadite is found in the oxidized zone of Mn-rich deposits and might be a major phase in ocean Mn nodules and crusts (Chukrov et al. 1987). Vernadite often is assumed to be analogous to the synthetic phase δ-MnO_2 (Villalobos et al. 2003; Grangeon, 2010; Lee et al. 2019), although the term δ-MnO_2 has been applied very broadly in recent years. Some have suggested that its formation is primarily mediated by biota (Chukrov et al. 1987; Grangeon et al. 2012). Unpolarized and polarized Raman spectra for vernadite from a Pacific Ocean crust (Table 1) contain a few broad peaks consistent with its disordered nature (Fig. 15).

Lithiophorite and Asbolane

Lithiophorite is constructed of stacked sheets of MnO_6 octahedra alternating with sheets of $Al(OH)_6$ octahedra in which one-third of the octahedra are vacant (Fig. 1). In the idealized structure, Li^+ cations fill the vacancies in the Al layer, and charge balance is maintained by Mn^{3+} replacing one-third of the Mn^{4+} cations (Post and Appleman 1994). The layers are cross-linked by H-bonds between the hydroxyl H^+ ions on the Al/Li layer and O atoms in the MnO_6 octahedra sheet. Chemical analyses show that transition elements such as Ni, Co, and Cu commonly substitute into the structure. Reported Li concentrations range from 0.2 to 3.3 weight % oxide (Ostwald 1984). Lithiophorite typically occurs in oxidized zones of Mn deposits and in some soils.

Polarized Raman spectra collected for lithiophorite (Fig. 16) show strong polarization effects for the higher frequency peaks, similar to that observed for most other phyllomanganates. The Raman spectra for lithiophorite from South Africa showed a curious for wavelengths of 514.5, 532, 633, and 785 nm laser light (Figs. 16 and 17), where Raman mode frequencies increase by 10 to 30 cm^{-1} as laser wavelengths became shorter. One possible explanation for the shift is that the shorter wavelength laser light oxidizes some of the Mn^{3+} to Mn^{4+}. We did not see this effect for other lithiophorite, or phyllomanganate samples. The large broad band centered near 340 cm^{-1} in the relatively weak 785 nm spectrum may be due to luminescence effects and appears to overwhelm the Raman mode near 380 cm^{-1} seen in the shorter laser wavelength spectra. This feature was especially prominent for the South African lithiophorite and less obvious in 785 nm spectra for other lithiophorite samples. It is possible that the cause of the luminescence is trace impurities unique to this sample. It also could be an orientation effect, as this is the only samplethat consisted of large plate-like crystals, which were oriented with their flat surface perpendicular to the laser beam. Other lithiophorite samples typically were fine-grained with random crystal orientations.

Because lithiophorite has alternating layers of $(Mn^{4+},Mn^{3+})\ O_6$ and $(Al,Li)O_6$ octahedral sheets, the structure contains a variety of octahedral environments: 1) Mn^{4+} in two-thirds of the Mn octahedra, with average Mn-O distances of ~1.89 Å (Post and Appleman 1994); 2) Jahn-Teller distorted Mn^{3+} octahedra in one-third of the Mn sites, with average Mn-O distances of ~2.04 Å (Shannon 1976); and 3) two-thirds $Al(OH)_6$ and one-third $Li(OH)_6$ in the Al,Li octahedral sheet, with Al-OH = 1.88 Å and Li-OH = 2.10 Å (Shannon 1976). This range of octahedral environments likely contributes to the typically broader peaks in the spectra for lithiophorite compared with those for chalcophanite. The lithiophorite spectra show no clear features below 350 cm^{-1}, presumably because there are no interlayer cations or water molecules, as there are in birnessite and chalcophanite phases.

LD calculations for lithiophorite (Fig. 18) indicate that A_{1g} modes above 500 cm^{-1} are due to MnO_6 and $Al(OH)_6$ octahedral sheet compression-expansion motions parallel to the *c*-axis, whereas the higher frequency E_g modes are due to MnO_6 and $Al(OH)_6$ octahedral sheet shear motions perpendicular to the *c*-axis. Calculated modes below 500 cm^{-1} have major contributions from O-H stretches parallel to the *c*-axis (A_{1g}) and H translations within the *a-b* plane (E_g).

Asbolane is a lithiophorite-like phase with transition-metal cations such as Co, Cu and Ni replacing some of the Al, and possibly Mn (Chukhrov et al. 1982; Manceau et al. 1987). The asbolane structure has not been determined, but Chukhrov et al. (1982) propose that it likely has hexagonal symmetry, and the lithiophorite $Al(OH)_6$ layer is largely replaced by poorly structured "islands" of $(Co, Ni, Cu)O_6$ octahedra. Figure 19 shows that spectra for several asbolane samples (Table 1) are similar to that of lithiophorite; a major difference is that the peak near 540-560 cm^{-1} is relatively stronger for the asbolane spectra, increasing in intensity with greater Co concentrations. Burlet and Vanbrabant (2015), based on results from a peak-fitting procedure, suggested a correlation between certain peak positions and intensities and the compositions of asbolane-lithiophorite samples; they also observed an intensity increase for a peak at ~540 cm^{-1} for asbolane relative to lithiophorite.

Feitknechtite

The crystal structure for feitknechtite is not known. The formula is assumed to be MnOOH, and some have speculated that the structure consists of layered MnO_6 octahedra (Luo et al. 1996, Grangeon et al. 2017). Our XPS data (unpublished results) confirm that all Mn is trivalent. Natural feitknechtite samples typically include hausmannite, which presumably is an alteration product of the feitknechtite. Feitknechtite occurs as an intermediate phase in syntheses of birnessite by oxidation of $Mn(OH)_2$ (Min and Kim 2019), and also has been reported in biogenically precipitated Mn oxides (Mandernack et al. 1995). Polarized Raman spectra for synthetic feitknechtite shown in Figure 20, and unpolarized spectra collecting using different laser lines are compared in Figure 21.

DISCUSSION

Phase Identification

In a recent study, we concluded that when users employ appropriate data collection conditions, Raman spectroscopy is an effective tool for the identification and characterization of tunnel-structure Mn oxide phases (Post et al. 2020). The current work extends those conclusions to layer-structure Mn oxides. Raman spectra for the various layer structure Mn oxide phases are compared in Figure 22. As all phyllomanganates are constructed of similar MnO_6 octahedra, it is not surprising that there are general similarities among the spectra, especially in the region from ~300 to 665 cm^{-1} that is dominated by internal MnO_6 octahedra modes. The spectra have sufficiently unique characteristics, especially at frequencies below 500 cm^{-1}, to make it possible, in most cases, to identify specific phases. Additionally, the phyllomanganate spectra are distinctly different from large tunnel Mn oxide spectra (Fig. 23) as discussed below.

Recent studies have shown that Mn oxide minerals from a variety of nonmarine sources and in particular those assumed to form biogenically typically have layer or large-tunnel structures, or are mixtures of both (McKeown and Post 2001, Bargar et al 2009, Ling et al. 2020). Furthermore, laboratory experiments indicate that various environmental conditions transform phyllomanganates into tunnel structures, thereby significantly altering the reaction potentials for the Mn oxides in soils and sediments (Atkins et al. 2014, Grangeon et al. 2014, Yang et al. 2019). Routine Raman identification of specific tunnel or layer Mn oxides, even for fine-grained samples and mixtures, and surface coatings, can be critical to understanding and modeling their behaviors in a variety of natural settings.

The spectra plotted in Figure 23 suggest that a reliable method for distinguishing large tunnel and layer structures is the presence or absence of a moderate-to-strong Raman mode near 725-740 cm^{-1}; this peak is present for all tunnel structures with predominantly Mn^{4+}, especially for those with large tunnels, e.g. romanechite and todorokite, but is absent in all phyllomanganate spectra – even layer structures containing only Mn^{4+}, such as chalcophanite. This tunnel-structure marker peak is particularly strong when spectra are collected using 633 or 785 nm laser light. Post et al. (2020) suggested that this high frequency Mn-O stretch mode arises from Mn^{4+}-O bonds in rigid octahedral tunnel structure frameworks. Phyllomanganate octahedral sheets, on the other hand, are more elastic, softening the Mn-O stretches. This behavior becomes even more pronounced with the replacement of some Mn^{4+} by the larger Mn^{3+} or by vacancies.

As mentioned above, spectra collected from many phyllomanganates show strongly polarized features, with strong intensities in the VV (laser light polarization parallel to analyzer polarization direction) spectra, and weak intensities in the VH (laser light polarization perpendicular to analyzer polarization direction) spectra. This behavior is particularly evident at the highest frequencies that are dominated by internal MnO_6 octahedral motions. Spectra collected under similar conditions for large-tunnel structures, however, showed little or no polarization dependence (Post et al. 2020).

Mn Oxidation State

Post et al. (2020) concluded that Raman frequencies of certain internal MnO_6 octahedral modes vary as a function of $Mn^{3+}/(Mn^{4+}+Mn^{3+})$ ratio. Increasing concentrations of the larger, Jahn-Teller distorted $Mn^{3+}O_6$ octahedra cause a lengthening of the average Mn-O bond and a more distorted octahedral environment, thereby decreasing the associated vibrational frequencies. This is true in general for tunnel-structure Mn oxides, but is particularly true for the hollandite group minerals, where a linear relationship was found between $Mn^{3+}/(Mn^{4+}+Mn^{3+})$ ratio and frequency of the internal MnO_6 octahedral mode near 630 cm^{-1}.

In the present study of phyllomanganates, we similarly noted a strong linear correlation ($R^2 = 0.984$) between the $Mn^{3+}/(Mn^{4+}+Mn^{3+})$ ratios and the frequencies for certain internal MnO_6 octahedral modes (Fig. 24). The highest frequency mode for chalcophanite and ranciéite occur near 669 cm^{-1}. This mode is dominated by internal MnO_6 octahedral vibrations, and might be expected to appear at high frequencies for phases where all Mn is tetravalent. In contrast, one-third of the Mn in triclinic Na- and K-birnessite is trivalent, and the comparable modes for these phases were observed near 638 cm^{-1}. Cation exchange of triclinic Na-birnessite can significantly alter the Mn redox state. For example, substitution of interlayer Na^+ with Ca^{2+} (Elmi et al 2020) and H^+ (Sylvester et al. 1997) will significantly reduce the $Mn^{3+}/(Mn^{4+}+Mn^{3+})$ ratio (Ilton et al. 2016). In our Raman spectra of Ca- and H-birnessite, the internal MnO_6 octahedral mode peaks were shifted to higher frequencies relative to those for K-, Na-, and Li-birnessites. The high-frequency modes plot approximately along the same trend line, with some uncertainty arising from the broadness of the associated Raman peaks. Additionally, for certain phases, some or all the Mn^{3+} will be in the interlayer region above or below octahedral vacancies, and this different bonding environment will likely modify (broaden) some Raman features.

The observed correlation of $Mn^{3+}/(Mn^{4+}+Mn^{3+})$ with the highest frequency Raman modes suggests that Raman spectroscopy might be used to assess the approximate Mn^{3+} concentration for birnessite-like phases, or for comparing Mn oxidation state before and after, or monitoring during, certain types of reactions. It also offers the potential of using Raman spectroscopy to map differences in Mn oxidation state in environmental or other complex samples.

Birnessite Symmetry

There has been considerable interest in recent years in establishing methods to distinguish triclinic and hexagonal birnessite-like samples, as the structural symmetry correlates with the Mn^{3+} and Mn site vacancy concentrations, which determine certain types of chemical reactivities, and can be an indicator of the formation mechanism, e.g. biotic or abiotic (Tebo et al. 2004, Webb et al. 2005). Commonly, powder X-ray diffraction patterns of natural birnessites show only a few broad peaks resulting from small crystallite sizes or possibly long-range structural disorder that cannot provide definitive long- or short-range symmetry characterization. In recent years, some researchers used specific, although sometimes subtle, differences in X-ray absorption spectroscopy features to distinguish triclinic from hexagonal birnessite-like phases (e.g. Webb, 2005). Others use pair distribution function modeling to assess the symmetry and other structural details (Yang et al. 2019; Lee et al. 2019). A drawback of both approaches is that data must be collected using synchrotron sources. Additionally, the results are not always conclusive, and in most cases *in situ* measurements are not routine.

Our results suggest that Raman spectroscopy offers several advantages for determining the structural symmetry for birnessite-like phases. In addition to not requiring a synchrotron source, Raman spectroscopy routinely enables the investigation of samples *in situ* with ~1 µm spatial resolution. Moreover, several features robustly differentiate between the spectra for triclinic (Na-birnessite) and hexagonal birnessite (H- birnessite) phases (Fig. 11). The internal MnO_6 octahedral modes between 500 and 650 cm^{-1} correspond to at least three partially resolved peaks in the Na-birnessite spectrum, and typically less resolved for H-birnessite. The prominent, low-frequency peaks below 500 cm $^{-1}$ in the Na-birnessite spectrum are absent or significantly weaker, or shifted, for H-birnessite (Fig. 11). The position of the highest frequency mode for Na-birnessite is shifted to lower frequency by approximately 10 cm^{-1} relative to that for H-birnessite, reflecting the greater concentrations of Mn^{3+} in Na-birnessites. Additionally, Figure 11 shows that the relative intensities for the two highest frequency modes (at about 580-590 and 640-650 cm^{-1}) are reversed in the hexagonal and triclinic birnessites, as previously observed by Julien et al. (2003), Hsu (2011), Yang et al. (2015), Boumaiza (2019), and Bernardini (2019). These distinctly different spectra indicate that Raman spectroscopy, using the appropriate data collection conditions, is perhaps the most conclusive method for readily distinguishing triclinic from hexagonal birnessite. Furthermore, information derived from Raman peak frequencies, relative intensities, and widths provide opportunities to explore detailed structural variations among different birnessite-like phases beyond a simple triclinic or hexagonal designation. Our results complement the study by Ling et al. (2017) that demonstrated Fourier transform infra-red spectra effectively distinguish hexagonal and triclinic birnessite-like structures, but Raman offers the advantages of better resolved spectral features and *in situ* microanalyses.

Vernadite

Vernadite is reported as a major phase in ocean Mn nodules and crusts, and as indicated above, is widely assumed to be a birnessite-like phase for which the basal reflection is largely absent in powder X-ray diffraction patterns. The missing basal reflection is thought to arise either from turbostratically disordered layer stacking, from crystallites with so few layers that interference effects are minimized, or a combination of both of these factors. The phase is characterized by a diffraction pattern showing broad peaks at ~2.44 and 1.45 Å. Synthetic samples that exhibit similar XRD patterns are commonly referred to as δ-MnO_2 and are assumed to be analogues of vernadite. The unpolarized Raman spectrum from an ocean Mn crust that gave an XRD pattern consistent with vernadite is shown in Figure 25 along with spectra for hexagonal birnessite, synthetic δ-MnO_2, and asbolane. The natural vernadite spectrum most closely resembles that for asbolane, or perhaps a mixture of asbolane and hexagonal birnessite, and is distinctly different from that of δ-MnO_2 (Villalobos et al. 2003), which is more similar to that of hexagonal birnessite. This observation brings into question the assumption that δ-MnO_2 is always an appropriate analogue for vernadite. The issue is complicated by the fact that there are reported variations in composition, and presumably structures, for vernadites. In addition, different synthesis methods and treatments have been employed to produce "δ-MnO_2" phases, which are not always identical. Lee et al. (2019) concluded from their TEM and PDF studies of ocean crust vernadite that this phase is best modeled by interstratified structures with 7 and 10 Å interlayer spacings. Our preliminary results suggest that Raman spectroscopy is a useful tool for characterizing and comparing similarities and differences among natural vernadites and synthetic δ-MnO_2 phases. More in-depth Raman studies of a range of natural and synthetic vernadite-like phases is ongoing.

IMPLICATIONS

We present here a comprehensive Raman spectroscopy study of layer structure Mn oxide phases from a large assortment of well-characterized natural and synthetic samples, using a variety of data collection conditions (Fig. 22). We demonstrate here and in our previous study of tunnel structure Mn oxides that when using multiple lasers, especially at 785 and 633 nm wavelengths, with low laser powers at the sample (30 – 500 µW, depending upon the laser wavelength and the sample), we were able to consistently identify the Mn oxide phases for most samples. In particular, it is routinely possible to distinguish phases with large tunnels from those with layers (Fig. 23). Additionally, for birnessite-like phases, we observed that the position of the highest frequency Raman mode correlates with $Mn^{3+}/(Mn^{4+}+ Mn^{3+})$, suggesting that Raman spectroscopy might be an effective tool for assessing approximate absolute and relative Mn^{3+}concentrations in this important group of phyllomanganates. With the comprehensive Raman database of well-characterized Mn oxide standards from Post et al (2020), and provided here and as supplementary data[1] with the *American Mineralogist*, micro-Raman is a powerful tool for identification and characterization of biotic and abiotic Mn oxide phases from diverse natural settings, and thereby can provide new insights into the roles of these phases in our environment and on other planets. Current plans for the next NASA Mars lander include a Raman system, where one of the primary targets will be black rock coatings that resemble rock varnishes on Earth (Marnocha 2017). As Mn oxides in terrestrial varnishes are thought to be biologically precipitated (McKeown and Post 2001; Northup et al. 2010; Marnocha and Dixon 2014), Raman identification of similar appearing Mn oxide minerals on Mars might be interpreted as indicators of past or possibly current biotic processes on Mars (Marnocha 2017). A comprehensive database of high-quality Raman spectra from well-characterized Mn oxide minerals will be useful for such Martian studies. Additionally, the method is equally applicable for identification and characterization of laboratory produced Mn oxides and those used industrially.

ACKNOWLEDGEMENTS

We are grateful for the invaluable assistance provided by Rob Wardell with the operation of the Raman laboratory in the Smithsonian Department of Mineral Sciences and Maxwell Wetherington in the Raman laboratory of the Materials Characterization Laboratory, Penn State University. Florence T. Ling kindly allowed us to analyze a suite of birnessite samples that she synthesized. Funding for this work was provided by NSF Grant EAR-1925903

REFERENCES CITED

Atkins, A.L., Shaw, S., and Peacock, C.L. (2014) Nucleation and growth of todorokite from birnessite: Implications for trace-metal cycling in marine sediments. Geochimica et Cosmochimica Acta, 144, 109-125.

Bargar, J.R., Fuller, C.C., Marcus, M.A., Brearley, A.J., De la Rosa, M.P., Webb, S.M. and Caldwell, W.A. (2009). Structural characterization of terrestrial microbial Mn oxides from Pinal Creek, AZ. Geochimica et Cosmochimica Acta, 73, 889-910.

Bernard, M., Hugot-Le Goff, A., and Thi, B.V. (1993) Electrochromic reactions in manganese oxides. Journal of the Electrochemical Society, 140, 3065-3070.

Bernardini, S., Bellatreccia, F., Municchia, A.C.,Ventura, G.D., and Sodo, A. (2019) Raman spectra of natural manganese oxides. Journal of Raman Spectroscopy, 1-16.

Betekhtin, A.,G. (1940) Southern Ural manganese deposits as a resource base for the Magnitogorsk Metallurgical Trust, Trudi Institute of Geological Sciences. Academy of Sciences. USSR. no. 4.

Boumaiza, H., Renard, A., Robinson, M.R., Kervern, G., Vidal, L., Ruby, C., Bergaoui, L., and Coustel, R. (2019) A multi-technique approach for studying Na triclinic and hexagonal birnessites. Journal of Solid State Chemistry, 272, 234-243.

Bricker, 0. (1965) Some stability relations in the system $Mn0_2$ at 25° and one atmosphere total pressure. American Mineralogist, 50, 1296-1354.

Burlet, C. and Vanbrabant, Y. (2015) Study of the spectro-chemical signatures of cobalt–manganese layered oxides (asbolane–lithiophorite and their intermediates) by Raman spectroscopy. Journal of Raman Spectroscopy, 46, 941-952.

Buser, W., Graf, P, and Feitkecht, W. (1954) Beitrag zur Kenntnis der Mangan(II)-manganite und des δ-MnO_2. Helvetica chimica acta, 37, 2322-2333.

Chukhrov, F. V., Gorshkov, A. I., Rudnitskaya, Yeo S., et al. (1978) Vemadite. Izvestiya AN SSSR, seriya geologicheskay *a,* 6, 5-19.

Chukhrov, F.V., Gorshkov, A.L., Vitovskaya, Lv. Drits, V.A. and Sntsov, A.V. (1982) On the Nature of Co-Ni Asbolane; a Component of Some Supergene Ores. In Ore Genesis, G. C. Amstutz et al. (eds.), Springer-Verlag Berlin Heidelberg, pp. 230-239.

Chukhrov, F.V., Drits, V.A., Gorshkov, A.1., Sakharov, B.A., and Dikov, Yu.P. (1987) Structural models of vernadite. International Geology Review, 29, 1337-1347.

Dowty, E. (1987) "Vibrational interactions of tetrahedra in silicate glasses and crystals", Physics and Chemistry of Minerals 14, 122-138.

Dowty, E. (2007) Vibratz2.0 software details available at: “www.shapesoftware.com”.

Drits, V.A., Silvester, E., Gorshkov, A.I., and Manceau, A. (1997) Structure of synthetic monoclinic Na-rich birnessite and hexagonal birnessite: I. Results from X-ray diffraction and selected-area electron diffraction. American Mineralogist, 82, 946–961.

Elmi, C., Post, J.E., Heaney, P.J., and Ilton, E.S. (2020) Effects of pH and Ca exchange on the structure and redox state of synthetic Na-birnessite. American Mineralogist. In Press.

Ertle et al. (2005) Ertl, A., Pertlik, F., Prem, M., Post, J.E., Kim, S.J., Brandstatter, F., and Schuster, R. (2005) Rancieite crystals from Friesach, Carinthia, Austria. European Journal of Mineralogy, 17, 163–172.

Fateley, W.G., Dollish, F.R., McDevitt, N.T., and Bentley, F.F., Infrared and Raman Selection Rules for Molecular and Lattice Vibrations: the Correlation Method, (Wiley, New York, 1972).

Feng, X.H., Liu, F., Tan, W.F., and Liu, X.W. (2004) Synthesis of Birnessite from the Oxidation of Mn^{2+} by O_2 in Alkali Medium: Effects of Synthesis Conditions. Clays and Clay Minerals, 52(2), 240-250.

Feng, X.H., Zhai, L.M., Tan, W.F., Liu, F., and He, J.Z. (2007) Adsorption and redox reactions of heavy metals on synthesized Mn oxide minerals. Environmental Pollution 147(2), 366-373.

Feng, M., Du, Q., Su, L., Zhang, G., Wang, G., Ma, Z., Gao, W., Qin, X., and Shao, G. (2017) Manganese oxide electrode with excellent electrochemical performance for sodium ion batteries by pre-intercalation of K and Na ions. Sci Rep, 7, 2219-2226.

Fischel, M.H., Fischel, J.S., Lafferty, B.J., and Sparks, D.L. (2015) The influence of environmental conditions on kinetics of arsenite oxidation by manganese-oxides. Geochemical Transactions, 16, 15-24.

Fischer, T.B., Heaney, P.J. and Post, J.E. (2018). Changes in the structure of birnessite during siderophore-promoted dissolution: A time-resolved synchrotron X-ray diffraction study. Chemical Geology, 476, 46-58.

Fleeger, C.R., Heaney, P.J., and Post, J.E. (2013) A time-resolved X-ray diffraction study of Cs exchange into hexagonal H-birnessite. American Mineralogist, 98, 671-679.

Frey, C.E., Wiechen, M., and Kurz, P. (2014) Water-oxidation catalysis by synthetic manganese oxides--systematic variations of the calcium birnessite theme. Dalton Transactions, 43, 4370-4379.

Ghodbane, O., Pascal, J.L., and Favier, F. (2009) Microstructural effects on charge-storage properties in MnO2-based electrochemical supercapacitors. Applied Materials & Interfaces, 2009. 1(5), 1130-1139.

Giovanoli, R. (1980) Vernadite is random-stacked birnessite. Mineralium Deposita, 14, 249-261.

Golden, D.C., Dixon, J.B., and Chen, C.C. (1986) Ion exchange, thermal trasformations, and oxidizing properties of birnessite. Clays and Clay Minerals, 34(5), 511-520.

Grangeon, S., Lanson, B., Miyata, N., Tani, Y. and Manceau, A. (2010). Structure of nanocrystalline phyllomanganates produced by freshwater fungi. American Mineralogist, 95, 1608-1616.

Grangeon, S., Manceau, A., Guilhermet, J., Gaillot, A., Lanson, M. (2012) Zn sorption modifies dynamically the layer and interlayer structure of vernadite. Geochimica et Cosmochimica Acta, 85, 302-313.

Grangeon S., Lanson B., and Lanson M. (2014) Solid-state transformation of nanocrystalline phyllomanganate into tectomanganate: influence of initial layer and interlayer structure. Acta Crystallographica B, 70, 828–838.

Grangeon, S., Warmont, F., Tournassat, C., Lanson, B., Lanson, M., Elkaïm, E., and Claret, F. (2017). Nucleation and growth of feitknechtite from nanocrystalline vernadite precursor. European Journal of Mineralogy, 29, 767-776.

Händel, M., Rennert, T., and Totsche, K.U. (2013) A simple method to synthesize birnessite at ambient pressure and temperature. Geoderma, 193-194, 117-121.

Hinkle, M.A.G., Flynn, E.D., and Catalano, J.G. (2016) Structural response of phyllomanganates to wet aging and aqueous Mn(II). Geochimica Et Cosmochimica Acta, 192, 220-234.

Hsu, Y. K., Chen, Y. C., Lin, Y. G., Chen, L. C., & Chen, K. H. (2011). Reversible phase transformation of MnO 2 nanosheets in an electrochemical capacitor investigated by in situ Raman spectroscopy. Chemical Communications, 47, 1252-1254.

Ilton, E.S., Post, J.E., Heaney, P.J., Ling, F.T. and Kerisit, S.N. (2016) XPS determination of Mn oxidation states in Mn (hydr) oxides. Applied Surface Science, 366, 475-485.

Jiao, F., and Frei, H. (2010) Nanostructured manganese oxide clusters supported on mesoporous silica as efficient oxygen-evolving catalysts. Chem Commun (Camb), 46(17), 2920-2.

Jones, L.H.P., and Milne, A.A. (1956) Birnessite, a new manganese oxide mineral from Aberdeenshire, Scotland. Mineralogical Magazine, 31, 283-288.

Julien, C., Massot, M., Baddour-Hadjean, R., Franger, S., Bach, S., and Pereira-Ramos, J.P. (2003) Raman spectra of birnessite manganese dioxides. Solid State Ionics, 159(3-4), 345-356.

Julien, C.M., Massot, M., and Poinsignon, C. (2004) Lattice vibrations of manganese oxides. Spectrochimica Acta Part A: Molecular and Biomolecular Spectroscopy, 60(3), 689-700.

Kim, H. and Stair, P.C. (2004) Bacterially produced manganese oxide and todorokite: UV Raman spectroscopic comparison, Journal of Physical Chemistry B, 108, 17019-17026.

Kim, S.J. (1991) New characterization of takanelite. American Mineralogist, 76, 1426-1430.

Kong, K.P., Fischer, T.B., Heaney, P.J., Post, J.E., Stubbs, J.E., and Eng, P.J. (2019). Mineralogical and geochemical constraints on chromium oxidation induced by birnessite. Applied Geochemistry, 108, 104365.

Kwon, K.D., Refson, K., and Sposito, G. (2013) Understanding the trends in transition metal sorption by vacancy sites in birnessite. Geochimica Et Cosmochimica Acta, 101, 222-232.

Landrot, G., Ginder-Vogel, M., Livi, K., Fitts, J.P., and Sparks, D.L. (2012) Chromium(III) oxidation by three poorly crystalline manganese(IV) oxides. 2. Solid phase analyses. Environ Sci Technol, 46(21), 11601-9.

Lanson, B., Drits, V.A., Silvester, E., and Manceau, A. (2000) Structure of H-exchanged hexagonal birnessite and its mechanism of formation from Na-rich monoclinic buserite at low pH. American Mineralogist, 85, 826–838.

Lee, S., Xu, H., Xu, W., and Sun, X. (2019) The structure and crystal chemistry of vernadite in ferromanganese crusts. Acta Crystallographica, B75, 591-598.

Le Goff, P., Baffier, N., Bach, S., and Pereira-Ramos, J.P. (1996) Synthesis, ion exchange and electrochemical properties of lamellar phyllomanganates of the birnessite group. Materials Research Bulletin, 31(1), 63-75.

Lefkowitz, J.P., Rouff, A.A., and Elzinga, E.J. (2013) Influence of pH on the reductive transformation of birnessite by aqueous Mn(II). Environmental Science & Technology, 47(18), 10364-71.

Li, Z., Wang, J., Wang, Z., Ran, H., Li, Y., Han, X., and Yang, S. (2012) Synthesis of a porous birnessite manganese dioxide hierarchical structure using thermally reduced graphene oxide paper as a sacrificing template for supercapacitor application. New Journal of Chemistry, 36(7), 1490-1495.

Ling, F.T., Post, J.E., Heaney, P.J., and Ilton, E.S. (2018) The relationship between Mn oxidation state and structure in triclinic and hexagonal birnessites. Chemical Geology, 479, 216-227.

Ling, F.T., Post, J.E., Heaney, P.J., Kubicki, J.D., and Santelli, C.M. (2017) Fourier-transform infrared spectroscopy (FTIR) analysis of triclinic and hexagonal birnessites. Spectrochimica Acta Part A:Molecular and Biomolecular Spectroscopy, 178, 32-46.

Ling, F.T., Post, J.E., Heaney, P.J., Santelli, C.M., Ilton, E.S., Burgos, W.D., and Rose, A.W. (2020) A multi-method characterization of natural terrestrial birnessites. American Mineralogist, 105, 833-847.

Lopano, C.L., Heaney, P.J., Post, J.E., Hanson, J., and Komarneni, S. (2007) Time-resolved structural analysis of K- and Ba-exchange reactions with synthetic Na-birnessite using synchrotron X-ray diffraction. American Mineralogist, 92(2-3), 380-387.

Lopano, C.L., Heaney, P.J. and Post, J.E. (2009) Cs-exchange in birnessite: Reaction mechanisms inferred from time-resolved X-ray diffraction and transmission electron microscopy. American Mineralogist, 94, 816-826.

Lopano, C.L., Heaney, P.J., Bandstra, J.Z., Post, J.E., and Brantley, S.L. (2011) Kinetic analysis of cation exchange in birnessite using time-resolved synchrotron X-ray diffraction. Geochimica et Cosmochimica Acta, 75, 3973-3981.

Luo, J., Segal, S.R., Wang, J.Y., Tian, Z.R., and Suib, S.L. (1996). Synthesis, characterization, and reactivity of feitknechtite. MRS Online Proceedings Library Archive, 431.

Manceau, A., Iorca, S.L., and Calas, G. (1987) Crystal chemistry of cobalt and nickel in lithiophorite and asbolane from New Caledonia. Geochimica et Cosmochimica Acta, 51, 105-113.

Manceau, A., Lanson, B., and Drits, V.A. (2002) Structure of heavy metal sorbed birnessite. Part III: Results from powder and polarized extended X-ray absorption fine structure spectroscopy. Geochimica Et Cosmochimica Acta, 66(15), 2639-2663.

Mandernack, K.W., Post, J.E., and Tebo, B.M. (1995) Manganese mineral formation by bacterial spores of the marine Bacillus, strain SG-1: evidence for the direct oxidation of Mn (II) to Mn (IV). Geochimica et Cosmchimica Acta, 59, 4393-4408.

Manning, B.A., Fendorf, S.E., Bostick, B., and Suarez, D.L. (2002) Arsenic(III) oxidation and arsenic(V) adsorption reactions on synthetic birnessite. Environmental Science & Technology, 36(5), 976-81.

Marnocha, C.L. (2017) Rock coatings and the potential for life on Mars. Elements, 13, 187-191

Marnocha C.L. and Dixon J.C. (2014) Endolithic bacterial communities in rock coatings from Kärkevagge, Swedish Lapland. FEMS Microbiology Ecology 90: 533-542

McKeown, D.A., and Post, J.E. (2001) Characterization of manganese oxide mineralogy in rock varnish and dendrites using X-ray absorption spectroscopy. American Mineralogist, 86, 701-713.

McKenzie, R.M. (1971) The Synthesis of birnessite, cryptomelane, and some other oxides and hydroxides of manganese. Mineralogical Magazine, 38(296), 493-502.

Min, S. and Kim, Y. (2019). Phase transition and surface morphological characteristics of Intermediate product feitknechtite according to aging time during the synthesis of birnessite. Journal of the Mineralogical Society of Korea, 32, 213-222.

Nam, K.W., Kim, S., Yang, E., Jung, Y., Levi, E., Aurbach, D., and Choi, J.W. (2015) Critical Role of Crystal Water for a Layered Cathode Material in Sodium Ion Batteries. Chemistry of Materials, 27, 3721-3725.

Nambu, M. and Tanida, K. (1971) New mineral takanelite. The Journal of the Japanese Association of Mineralogists, Petrologists and Economic Geologists, 65, 1-5.

Northup D.E. and 7 coauthors (2010) Diversity of rock varnish bacterial communities from Black Canyon, New Mexico. Journal of Geophysical Research: Biogeosciences 115: 1-19

Ostwald, J. (1984) Two varieties of lithiophorite in some Australian deposits. Mineralogical Magazine, 48. 383-388.

Post J.E. and Appleman D.E. (1988) Chalcophanite, $ZnMn_3O_7{\cdot}3H_2O$; new crystal-structure determinations. American Mineralogist. 73, 1401–1404.

Post J.E. and Appleman D.E. (1994) Crystal structure refinement of lithiophorite. American Mineralogist, 79, 370–374.

Post, J.E., Heaney, P.J., and Ertl, A. (2008) Rietveld refinement of the ranciéite structure using synchrotron powder diffraction data. Powder Diffraction, 23(01), 10-14.

Post, J.E., Heaney, P.J., and Hanson, J. (2002) Rietveld refinement of a triclinic structure for synthetic Na-birnessite using synchrotron powder diffraction data. Powder Diffraction, 17(3), 218-221.

Post, J.E., McKeown, D.A., and Heaney, P.J. (2020) Raman Spectroscopy study of Manganese Oxides – Tunnel Structures. American Mineralogist, In Press.

Post, J.E., and Veblen, D.R. (1990) Crystal structure determinations of synthetic sodium, magnesium, and potassium birnessite using TEM and the Rietveld method. American Mineralogist, 75, 477-489.

Post, J.E. (1999) Manganese oxide minerals: crystal structures and economic and environmental significance. Proceedings of the National Academy of Sciences of the United States of America, 96(7), 3447-54.

Santelli, C.M., Webb, S.M., Dohnalkova, A.C. and Hansel, C.M. (2011). Diversity of Mn oxides produced by Mn (II)-oxidizing fungi. Geochimica et Cosmochimica Acta, 75, 2762-2776.

Sauer, K., and Yachandra, V.K. (2002) A possible evolutionary origin for the Mn4 cluster of the photosynthetic water oxidation complex from natural MnO2 precipitates in the early ocean. Proceedings of the National Academy of Sciences of the United States of America, 99, 8631-8636.

Shannon, R.D. (1976) Revised Effective Ionic Radii and Systematic Studies of Interatomie Distances in Halides and Chaleogenides. Acta crystallographica. Section A, Foundations of crystallography 32, 751-767.

Shumlas, S.L., Singireddy, S., Thenuwara, A.C., Attanayake, N.H., Reeder, R.J., and Strongin, D.R. (2016) Oxidation of arsenite to arsenate on birnessite in the presence of light. Geochemical Transactions, 17, 5.

Silvester, E., Manceau, A. and Drits, V.A. (1997) Structure of synthetic monoclinic Na-rich birnessite and hexagonal birnessite: II. Results from chemical studies and EXAFS spectroscopy. American Mineralogist, **82**, 962 978.

Tan, H., Zhang, G.X., Heaney, P.J., Webb, S.M., and Burgos, W.D. (2010) Characterization of manganese oxide precipitates from Appalachian coal mine drainage treatment systems. Applied Geochemistry, 25(3), 389-399.

Tebo, B.M., Bargar, J.R., Clement, B.G., Dick, G.J., Murray, K.J., Parker, D., Verity, R., and Webb, S. M. (2004). Biogenic manganese oxides: properties and mechanisms of formation. Annual Reviews in Earth and Planetary Science, 32, 287-328.

Umena, Y., Kawakami, K., Shen, J. R. and Kamiya, N. (2011). Crystal structure of oxygen-evolving photosystem II at a resolution of 1.9 Å. Nature, 473, 55-60.

Villalobos, Mario, Toner, B., Bargar, J., & Sposito, G. (2003). Characterization of the manganese oxide produced by Pseudomonas putida strain MnB1. Geochimica et Cosmochimica Acta, 67, 2649–2662.

Wang, M.X., Wang, Y.P., Tan, W.F., Liu, F., Feng, X.H., and Koopal, L.K. (2010) Effect of 1-1 electrolyte concentration on the adsorption/desorption of copper ion on synthetic birnessite. Journal of Soils and Sediments, 10(5), 879-885.

Webb, S.M., Tebo, B.M. and Bargar, J.R. (2005). Structural characterization of biogenic Mn oxides produced in seawater by the marine Bacillus sp. strain SG-1. American Mineralogist, 90, 1342-1357.

Wiechen, M., Zaharieva, I., Dau, H., and Kurz, P. (2012) Layered manganese oxides for water-oxidation: alkaline earth cations influence catalytic activity in a photosystem II-like fashion. Chemical Science, 3(7), 2330-2339.

Witzke, T., Pöllmann, H., Gardolinski, J.E.F.C. and Sommariva,M. (2017) Lagalyite, IMA 2016, 106.

Yamaguchi, K., Shoji, M., Isobe, H., Yamanaka, S., Umena, Y., Kawakami, K. and Kamiya, N. (2017) On the guiding principles for understanding of geometrical structures of the CaMn4O5 cluster in oxygen-evolving complex of photosystem II. Proposal of estimation formula of structural deformations via the Jahn–Teller effects. Molecular Physics, 115, 636-666.

Yang, L.F., Cheng, S., Ji, X., Jiang, Y., Zhou, J., and Liu, M.L. (2015) Investigations into the origin of pseudocapacitive behavior of Mn_3O_4 electrodes using in operando Raman spectroscopy. Journal of Materials Chemistry A, 3(14), 7338-7344.

Yang, P., Post, J.E., Wang, Q., Xu, W., Geiss, R., McCurdy, P.R., and Zhu, M. (2019) Metal adsorption controls stability of layered manganese oxides. Environmental Science & Technology 53 (13), 7453-7462.

Yin, H., Liu, F., Feng, X., Hu, T., Zheng, L., Qiu, G., Koopal, L.K., and Tan, W. (2013) Effects of Fe doping on the structures and properties of hexagonal birnessites – Comparison with Co and Ni doping. Geochimica et Cosmochimica Acta, 117, 1-15.

Zhang, C., Chen, C., Dong, H., Shen, J. R., Dau, H. and Zhao, J. (2015) A synthetic Mn4Ca-cluster mimicking the oxygen-evolving center of photosynthesis. Science, 348, 690-693.

Zhao, H., Zhu, M., Li, W., Elzinga, E.J., Villalobos, M., Liu, F., Zhang, J., Feng, X., and Sparks, D.L. (2016) Redox Reactions between Mn(II) and Hexagonal Birnessite Change Its Layer Symmetry. Environmental Science & Technology, 50(4), 1750-8.

Endnote: 1Deposit item AM-XXXX, Supplemental Material. Deposit items are free to all readers and found on the MSA website, via the specific issue’s Table of Contents (go to http://www.minsocam.org/MSA/AmMin/TOC/20XX/XXXX_data/ XXXX_data.html).

FIGURE CAPTIONS

Figure 1. Polyhedral drawings of manganese oxide layer structures. The blue octahedra contain Mn; in chalcophanite, the green octahedra contain Zn, and for lithiophorite the magenta octahedra are 2/3 Al and 1/3 Li. The yellow spheres in the birnessite structure represent disordered Na atoms and water molecules.

Figure 2. Raman spectra (633 nm) for chalcophanite (NJ #C1814) with plate-like crystals (and MnO_6 octahedral sheets) perpendicular to incident laser light direction. Spectra are labeled Unpolarized (black), VV (blue), and VH (red). VV and VH spectra were collected using parallel and crossed polarization conditions, respectively.

Figure 3. Raman spectra for chalcophanite (NJ #C1814) collected using 532 (0.03 mW), 633 (0.05 mW) and 785 (0.11 mW) nm laser light. Spectra are rescaled and offset for clarity.

Figure 4. Raman spectra (532 nm) for chalcophanite (NJ #C1814), ernienickelite (#171561), and jianshuiite (MD) with plate-like crystals (and MnO_6 octahedral sheets) parallel to laser polarization (laser light direction perpendicular to plate-like crystals).

Figures 5a and b. Raman spectra (532 nm) for: a) chalcophanite (NJ #C1814) with crystals oriented with MnO_6 octahedral sheets parallel (top) and perpendicular (bottom) to the laser polarization direction, and b) chalcophanite (NJ #C1814) and ernienickelite (#171561) showing

OH stretch modes with the polarization symbol indicating laser polarization perpendicular to the MnO_6 octahedral sheets (or laser light direction parallel to MnO_6 octahedral sheets).

Figure 6a and b. a) Raman modes determined from lattice dynamics (LD) calculations for chalcophanite (#C1814) plotted as vertical lines below their respective Raman spectra (633 nm), and b) an eigenmode drawing of the highest calculated frequency Ag mode for chalcophanite: (110) projection with the c-axis vertical, showing MnO_6 octahedral deformation, O-Mn-O bend and Mn-O stretch, and Zn-O stretch with Zn translating along the c-axis.

Figure 7. Raman spectra (633 nm) for rancieite (#128319) with plate-like crystals (and MnO_6 octahedral sheets) perpendicular to incident laser light direction. Spectra labeled VV and VH were collected using parallel and crossed polarization conditions, respectively.

Figure 8. Raman spectra for rancieite (#128319) collected using 532 (0.03 mW), 633 (< 0.1 mW) and 785 (0.11 mW) nm laser light. Spectra are rescaled and offset for clarity.

Figure 9. Raman spectra (785 nm) for a variety of different rancieite specimens. Locations and specimen numbers are indicated (see Table 1). Samples were flattened such that MnO_6 octahedral sheets were perpendicular to incident laser light direction. Spectra are rescaled and offset for clarity.

Figure 10. Raman modes determined from LD calculations for rancieite (#128319) plotted as vertical lines below their respective Raman spectra (633 nm laser light).

Figure 11a. and b. Raman spectra for synthetic triclinic Na-birnessite and synthetic hexagonal birnessite, with plate-like crystals (and MnO_6 octahedral sheets) perpendicular to incident laser light direction, using a) 633 nm and b) 785 nm laser light. Spectraare rescaled and offset for clarity.

Figure 12a. and b. a) Raman spectra for Na-birnessite collected using 532 (0.03 mW), 633 (< 0.1 mW) and 785 (0.11 mW) nm laser light, and b) Raman spectra (633 nm) for Na-birnessite using different laser power levels at the sample (each measurement was from a different, but nearby point on the sample). Sample alteration is evident at incident powers above 0.1 mW. Sample alteration at 0.15 mW can result in different mixtures of phases as shown for two different points on the sample. Spectra are rescaled and offset for clarity.

Figure 13. Na-birnessite Raman modes determined from LD calculations for the simplified C2/m monoclinic structure plotted as vertical lines below their respective Raman features in the 785 nm spectrum.

Figure 14. Raman spectra (785 nm) for a variety of synthetic birnessite specimens with different interlayer cations (see Table 1). Samples were flattened such that MnO_6 octahedral sheets were perpendicular to incident laser light direction. Spectra are rescaled and offset for clarity.

Figure 15. Raman spectra (633 nm) for vernadite (Pacific ocean crust), with plate-like crystals (and MnO_6 octahedral sheets) perpendicular to incident laser light direction. Spectra labeled VV and VH were collected using parallel and crossed polarization conditions, respectively.

Figure 16. Polarized Raman spectra (514.5 nm) for lithiophorite (#162391), with plate-like crystals (and MnO_6 octahedral sheets) perpendicular to incident laser light direction and parallel to the laser polarization. Spectra labeled VV and VH were collected using parallel and crossed polarization conditions, respectively.

Figure 17. Raman spectra for lithiophorite (#162391) collected using 532 (0.03 mW), 633 (< 0.1 mW) and 785 (0.11 mW) nm laser light. Spectra are rescaled and offset for clarity.

Figure 18. Raman modes determined using lattice dynamics (LD) calculations for lithiophorite (#162391) structure; the calculated mode frequency for each mode is plotted as a vertical line below their respective Raman spectra (514.5 nm laser light).

Figure 19. Raman spectra (785 nm laser light) for a variety of different asbolane specimens (Table 1). The Co/Mn (Table 1) in the samples increases from the top to bottom spectrum. Spectra are rescaled and offset for clarity.

Figure 20. Raman spectra (633 nm) for synthetic feitknechtite. Spectra labeled VV and VH were collected using parallel and crossed polarization conditions, respectively.

Figure 21. Raman spectra for feitknechtite collected using 532 (0.03 mW), 633 (< 0.1 mW) and 785 (0.11 mW) nm laser light. Spectra are rescaled and offset for clarity.

Figure 22. Raman spectra for a variety of phyllomanganates, ordered from top to bottom according to decreasing Mn3+/(Mn4++Mn3+). Specimens measured are: chalcophanite (R12334), rancieite Austria, synthetic Ca-birnessite, synthetic Na-birnessite, synthetic hexagonal birnessite, and lithiophorite (162391) (Table 1). Spectra are rescaled and offset for clarity.

Figure 23. Raman spectra for a variety of layer- and tunnel-structure Mn oxide phases. Tunnel structure Mn-oxide spectra originally presented in the tunnel Mn-oxide study, Post et al. (2020); samples: cryptomelane (NMNH 89104), romanechite (NMNH R2232), todorokite (HU 126232). Layer structure spectra from: chalcophanite (R12334), rancieite Austria, synthetic Na-birnessite, synthetic hexagonal birnessite, and lithiophorite (162391). Spectra are rescaled and offset for clarity.

Figure 24. $Mn^{3+}/(Mn^{3+}+Mn^{4+})$ ratio versus Raman shift frequency of the highest frequency vibrational mode for the different phyllomanganates included in this study.

Figure 25. Raman spectra (785 nm) for vernadite (Pacific ocean crust), asbolane (#103709), synthetic hexagonal birnessite (pH 2), and synthetic δ-MnO_2. Spectra are rescaled and offset for clarity.

Table 1 Specimens used for Raman Spectroscopy

Mineral	**Specimen #**	**Locality**	**Chemical Formula**
Chalcophanite	C1814	Sterling Hill mine, NJ	$ZnMn_3O_7 \cdot 3H_2O$
	R12334	Bisbee, AZ	$ZnMn_3O_7 \cdot 3H_2O$
Ernienickelite	171561	Kalgoorlie-Boulder Shire, Australia	$NiMn_3O_7 \cdot 3H_2O$
Jianshuiite		Medford Quarry, MD	$MgMn_3O_7 \cdot 3H_2O$

Rancieite		Friesach, Austria	$Ca_{0.19}K_{0.01}(Mn^{4+}_{0.91}\,\square_{0.09})O_2 \cdot 0.63H_2O$
	128318	Rancie Mtn., France	$Ca_{0.14}\,Mg_{.04}Ba_{.01}K_{0.01}(Mn^{4+}_{0.87}\,Zn_{.06}\square_{0.07})O_2 \cdot 0.63H_2O$
	29.74	Alsace, France	$Ca_{0.16}\,Mg_{.01}Ba_{.01}K_{0.01}(Mn^{4+}_{0.91}\,\square_{0.09})O_2 \cdot 0.63H_2O$
		Spain	$Ca_{0.13}\,Mg_{.04}Ba_{.02}K_{0.01}(Mn^{4+}_{0.91}\,\square_{0.09})O_2 \cdot 0.63H_2O$
Na-birnessite		Synthetic[a]	$Na_{0.58}(Mn^{4+}_{1.34}Mn^{3+}_{0.66})\,O_4 \cdot 1.4H_2O$
K-birnessite		Synthetic[a]	$K_{0.58}(Mn^{4+}_{1.34}Mn^{3+}_{0.66})\,O_4 \cdot 1.4H_2O$
Li-birnessite		Synthetic[a]	$Li_{0.58}(Mn^{4+}_{1.34}Mn^{3+}_{0.66})\,O_4 \cdot 1.4H_2O$
Ba-birnessite		Synthetic[a]	$Ba_{0.29}(Mn^{4+}_{1.34}Mn^{3+}_{0.66})\,O_4 \cdot 1.6H_2O$
Ca-birnessite		Synthetic[a]	$Ca_{0.30}(Mn^{4+}_{1.34}Mn^{3+}_{0.50}\square_{0.16})\,O_4 \cdot 1.6H_2O$
Hex-birnessite		Synthetic (pH 2)[b]	$Mn^{3+}_{0.2}(Mn^{4+}_{1.34}Mn^{3+}_{0.66}\square_{0.09})\,O_4 \cdot 1.6H_2O$
Vernadite		Pacific Ocean crust	$Na_{0.47}Ca_{.28}Mg_{.16}\,K_{0.03}\,(Fe_{1.18}Si_{.28}Al_{.07}Ti_{.09}\square)(Mn^{4+},Mn^{3+})_2\,O_4 \cdot nH_2O$
δ-MnO_2		Synthetic[c]	$(Na_{.09}Mn^{3+}_{.08}K_{.07})(Mn^{4+}_{.70}Mn^{3+}_{.26}\square_{.04})O_2 \cdot nH_2O$
Feitknechtite[d]		Synthetic	$Mn(OH)_3$ (assumed)
Lithiophorite	162391	Postmasburg, South Africa	$(Al_{0.67}Li_{0.33})(Mn^{4+}_{0.67}Mn^{3+}_{0.33})O_2(OH)_2$
		Georgia, USA	$(Al_{0.80}Co_{0.08})(Mn)O_2(OH)_x$
	46158	Rengersdorf, Germany	$(Al_{.75}Si_{.09}Co_{.06}Ni_{.03})MnO_2(OH)_x$
Asbolane	97579	Kasaigaigori, Japan	$(Al_{.79}Co_{.34}Fe_{.04})MnO_2(OH)_x$

	103709	La Motte mi., Missouri	$(Co_{.69}Cu_{.24}Ni_{.10}Zn_{.04}Al_{.04})MnO_2(OH)_x$
	R2247	Sachsen, Germany	$(Al_{.78}Co_{.14}Fe_{.22})MnO_2(OH)_x$
	R9752	Schneeberg, Germany	$(Al_{.47}Co_{.04}Fe_{.05})MnO_2(OH)_x$

a –Na-birnessite synthesized and sample exchanged with respective interlayer cation following method of Golden et al (1986)

b – Hexagonal birnessite formed by reacting Na-birnessite with pH 2 HCl solution.

c – sample provided by M. Zhu, synthesized using method of Villilobos et al. (2003)

d – sample provided by E. Elzinga

Note: Li content for lithiophorite from South Africa determined by single crystal X-ray structure refinement by Post and Appleman (1994); Li concentrations were not determined for other lithiophorite and asbolane samples. Asbolane cation values were normalized to one Mn.

Table 2. Factor group analysis (FGA) results of the tunnel structure-type Mn-oxides phases. Γ_{optic} includes Raman- and IR-active modes; three $\Gamma_{acoustic}$ modes are indicated for each phase. The space group of each phase are listed in Hermann-Mauguin notations.

Phase	**Space Group:**	**FGA**
Lithiophorite	R-3m (#166)	$\Gamma = 3A_{1g} + 3E_g + 5A_{2u} + 5E_u$ $\Gamma_{Acoustic}$: $A_{2u}(z) + E_u(xy)$
Chalcophanite	R-3 (#148)	$\Gamma = 14A_g + 14E_g + 14A_u + 14E_u$ $\Gamma_{Acoustic}$: $A_u(z) + E_u(xy)$
Na-Birnessite	C-1 (#2)	$\Gamma = 6A_g + 6A_u$ $\Gamma_{Acoustic}$: $3A_g$
Rancieite	P -3	$\Gamma = 5A_g + 5E_g + 5A_u + 5E_u$ $\Gamma_{Acoustic}$: $A_u + E_u$

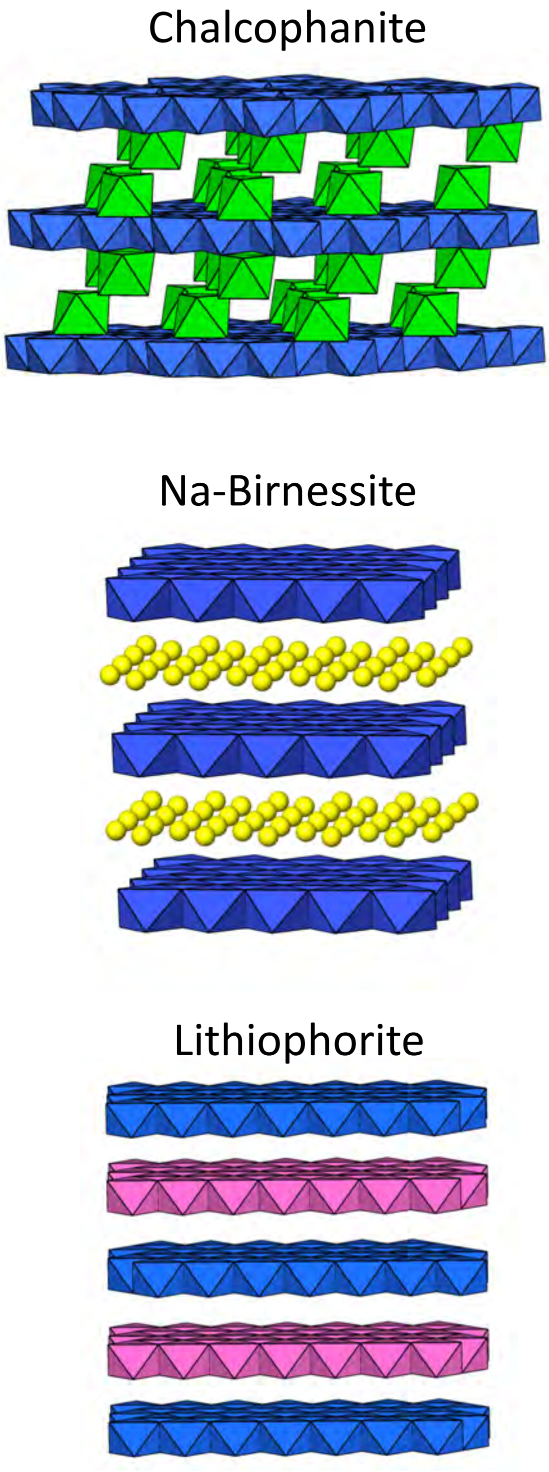

Figure 1

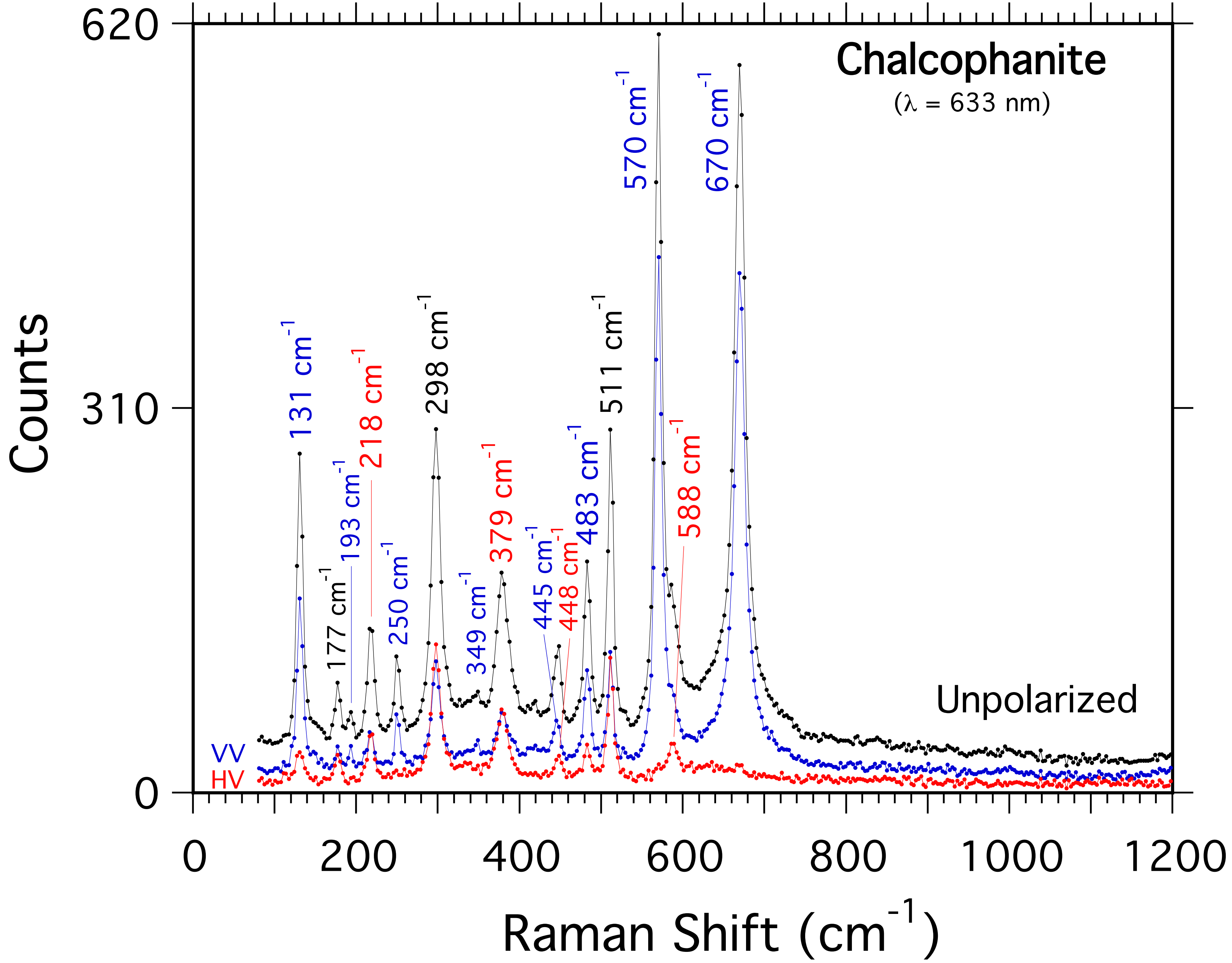

Chalcophanite
(λ = 633 nm)
Counts
620
310
0
Raman Shift (cm^-1)
0
200
400
600
800
1000
1200
131 cm^-1
177 cm^-1
193 cm^-1
218 cm^-1
250 cm^-1
298 cm^-1
349 cm^-1
379 cm^-1
445 cm^-1
448 cm^-1
483 cm^-1
511 cm^-1
570 cm^-1
588 cm^-1
670 cm^-1
Unpolarized
VV
HV

Fig. 2

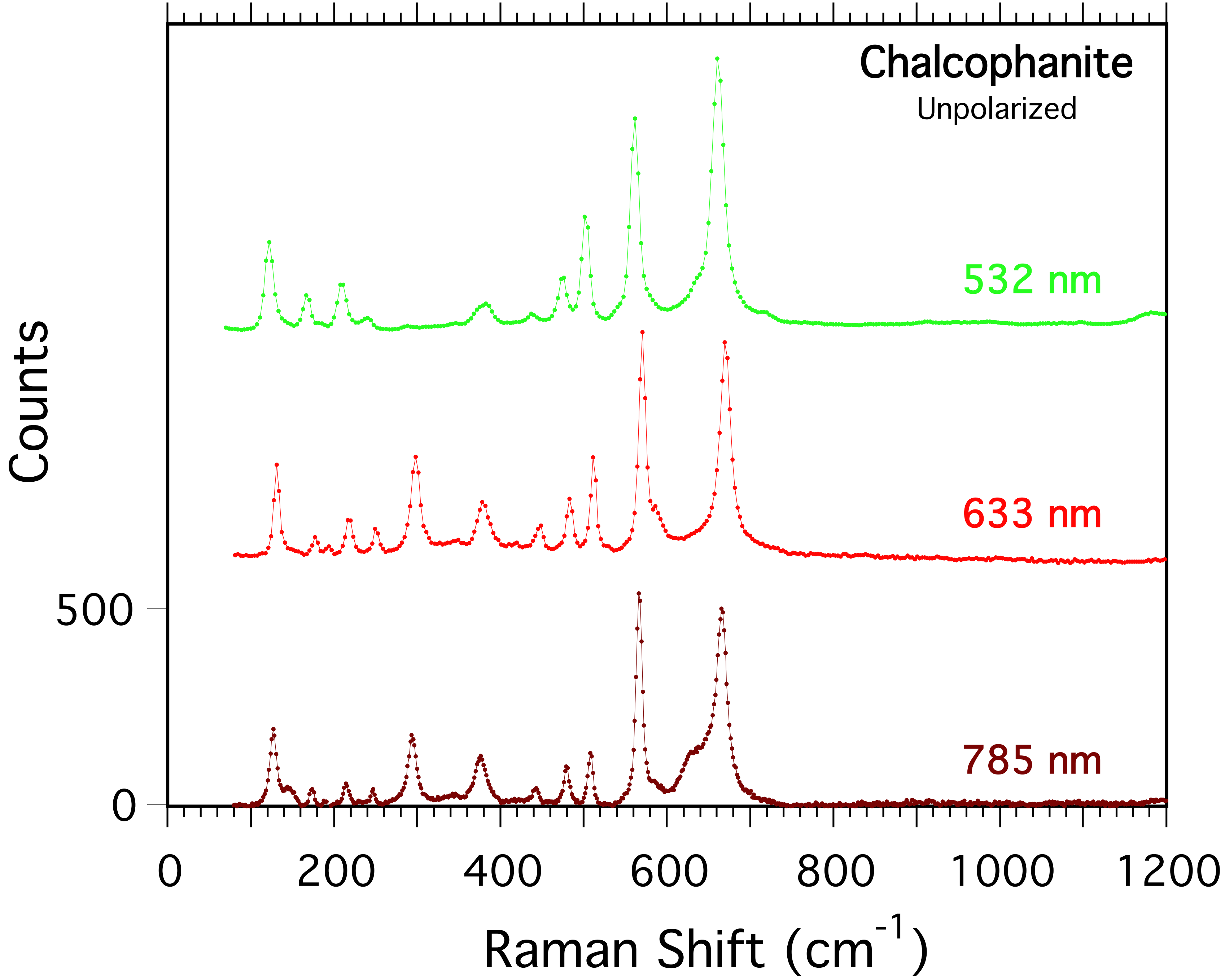
Chalcophanite
Unpolarized
532 nm
633 nm
785 nm
Counts
500
0
0
200
400
600
800
1000
1200
Raman Shift (cm^{-1})

Fig. 3

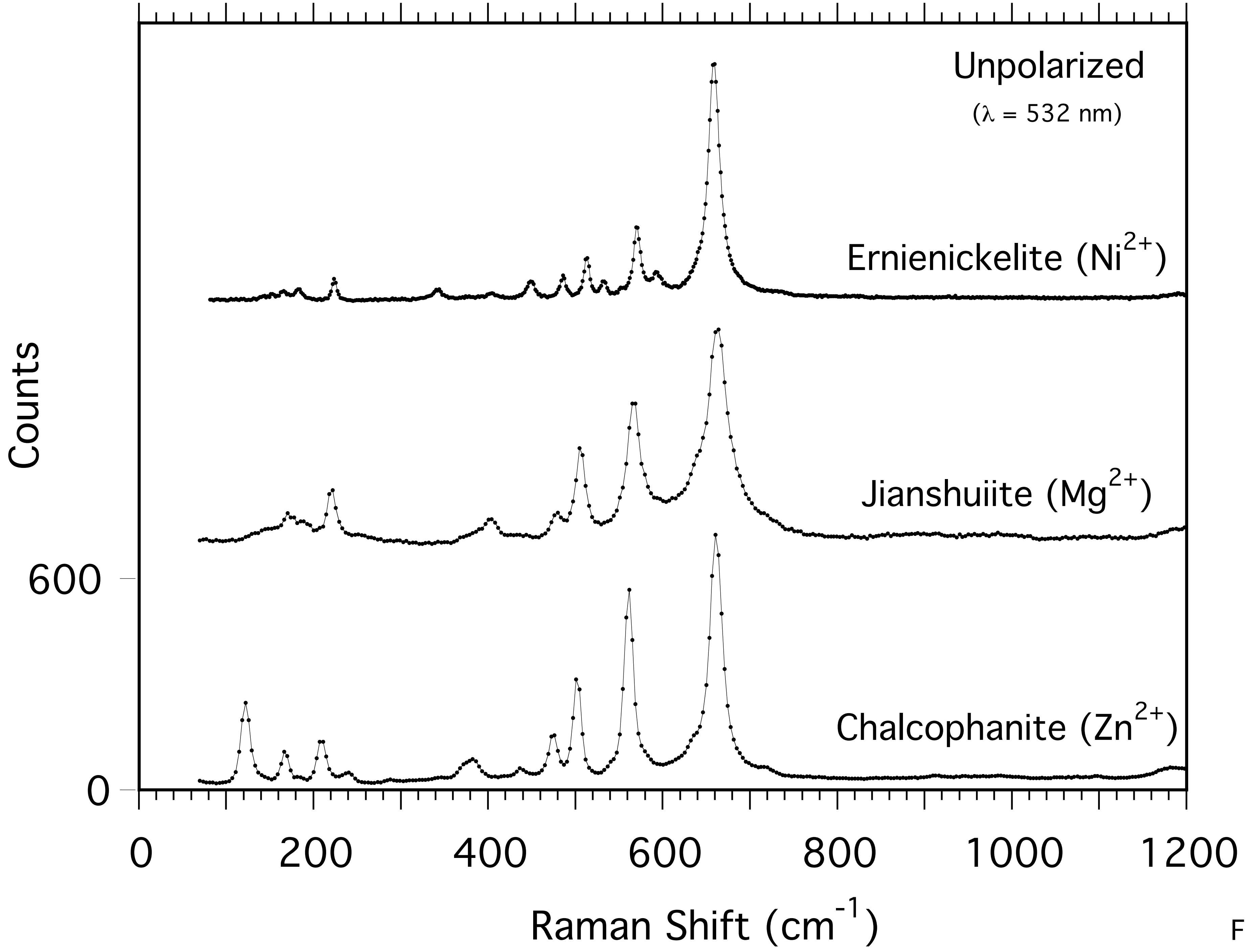
Unpolarized
(λ = 532 nm)
Ernienickelite (Ni2+)
Jianshuiite (Mg2+)
Chalcophanite (Zn2+)
Counts
600
0
0
200
400
600
800
1000
1200
Raman Shift (cm-1)

Fig. 4

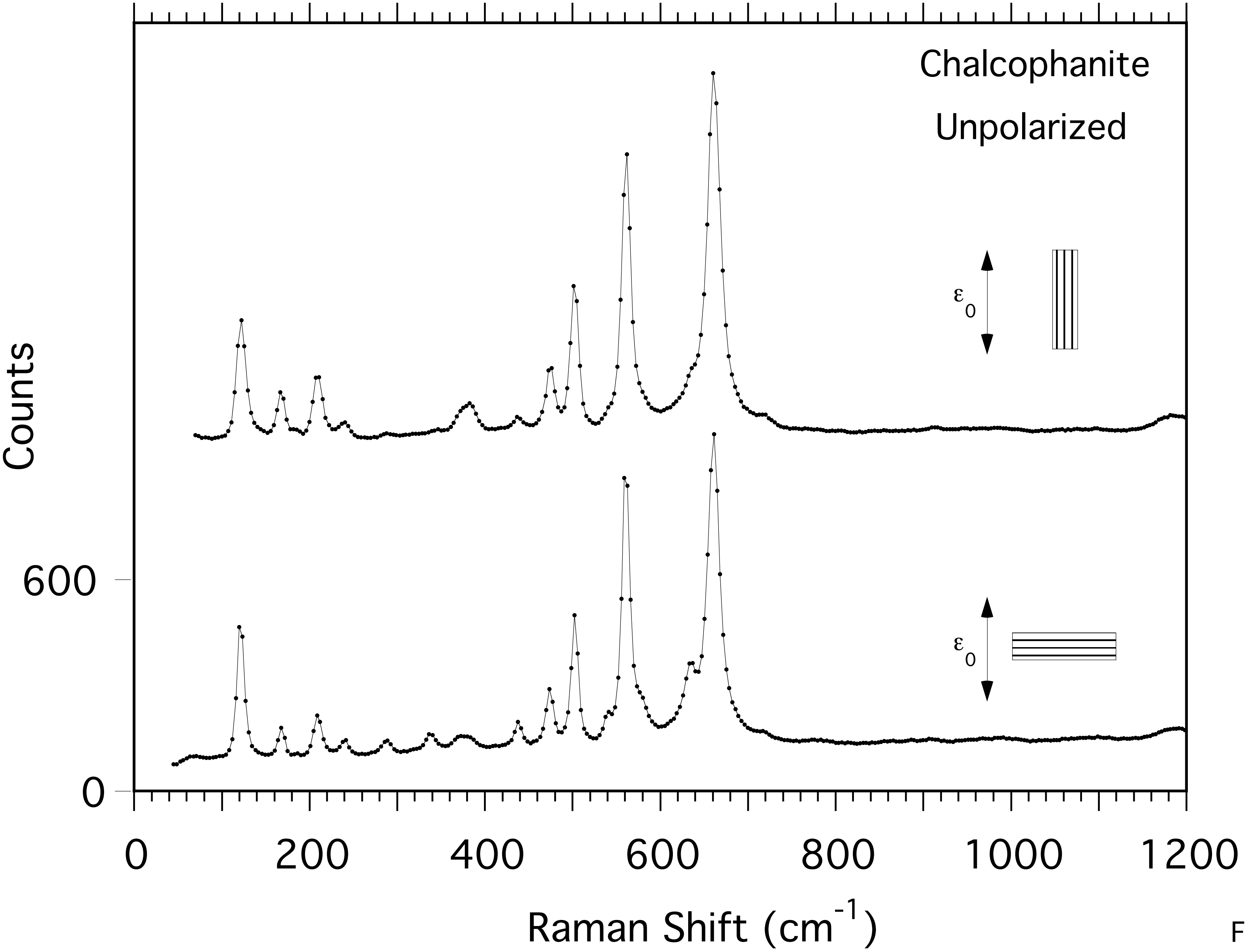
Chalcophanite
Unpolarized
ε_0
ε_0
Counts
600
0
0
200
400
600
800
1000
1200
Raman Shift (cm^{-1})

Fig. 5a

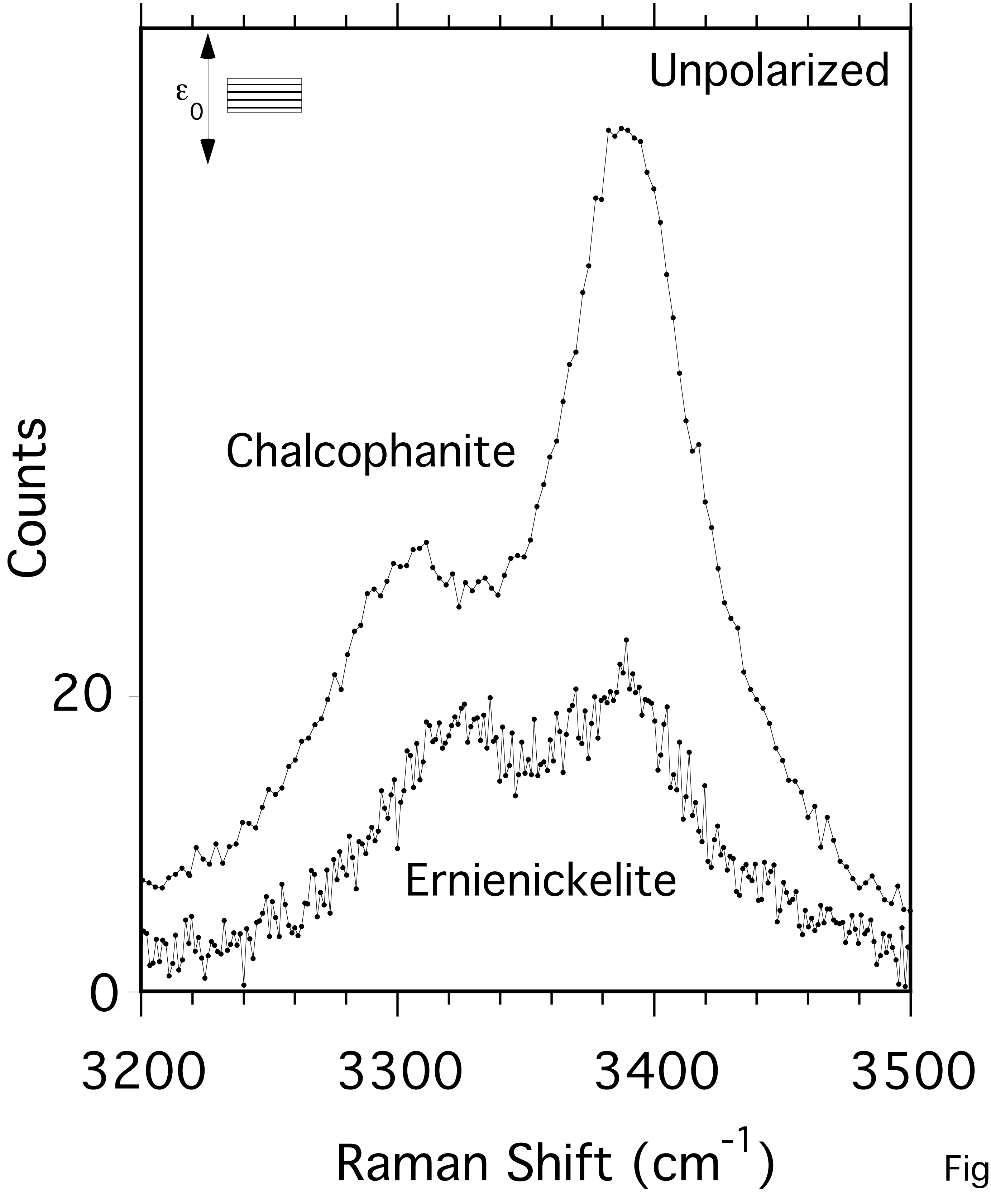
Unpolarized
ε_0
Chalcophanite
Ernienickelite
Counts
20
0
3200
3300
3400
3500
Raman Shift (cm^{-1})

Fig. 5b

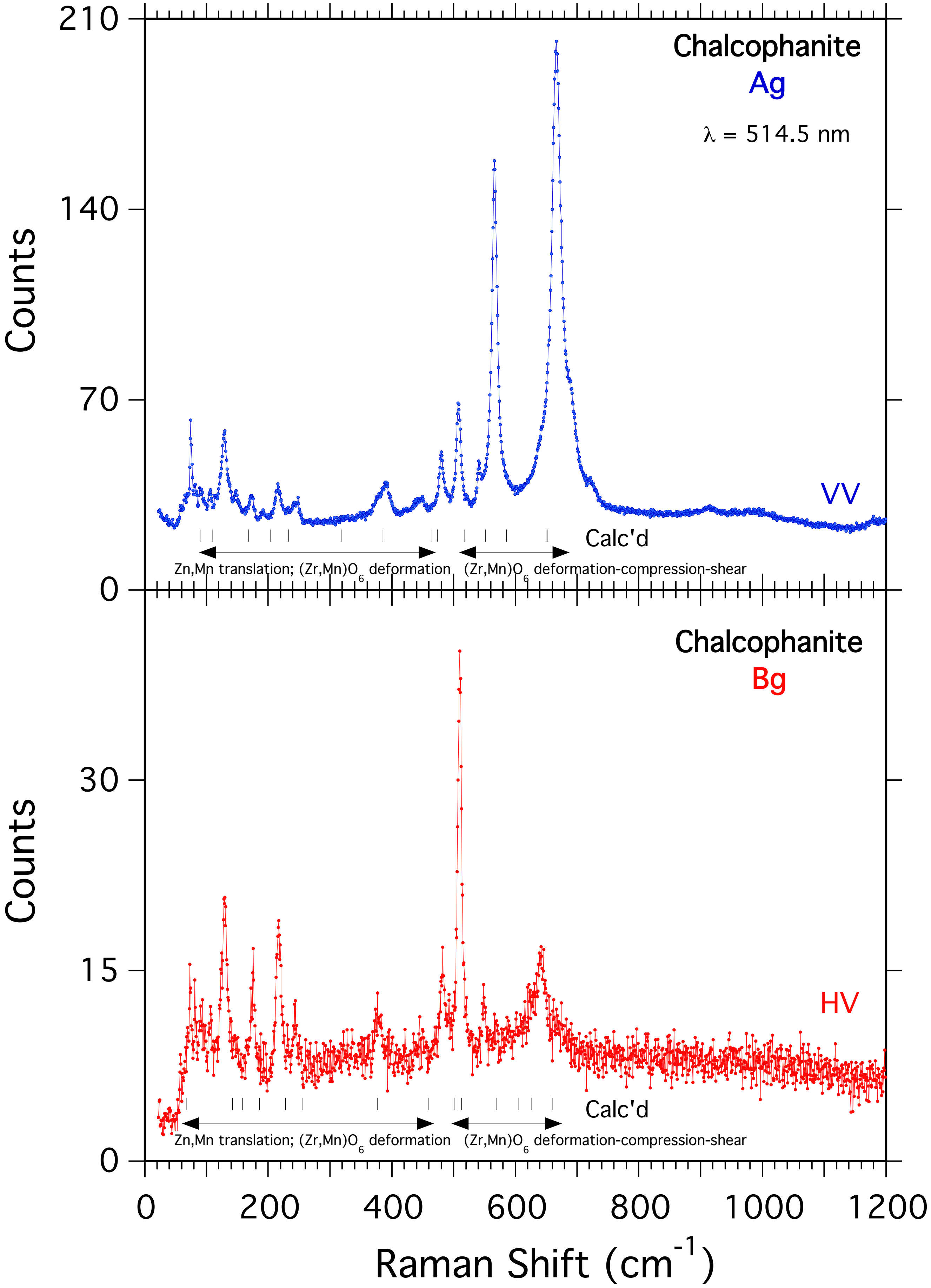
Chalcophanite
Ag
λ = 514.5 nm
VV
Calc'd
Zn,Mn translation; (Zr,Mn)O$_6$ deformation
(Zr,Mn)O$_6$ deformation-compression-shear
Chalcophanite
Bg
HV
Calc'd
Zn,Mn translation; (Zr,Mn)O$_6$ deformation
(Zr,Mn)O$_6$ deformation-compression-shear
Counts
210
140
70
0
Counts
30
15
0
0
200
400
600
800
1000
1200
Raman Shift (cm^{-1})

Fig. 6a

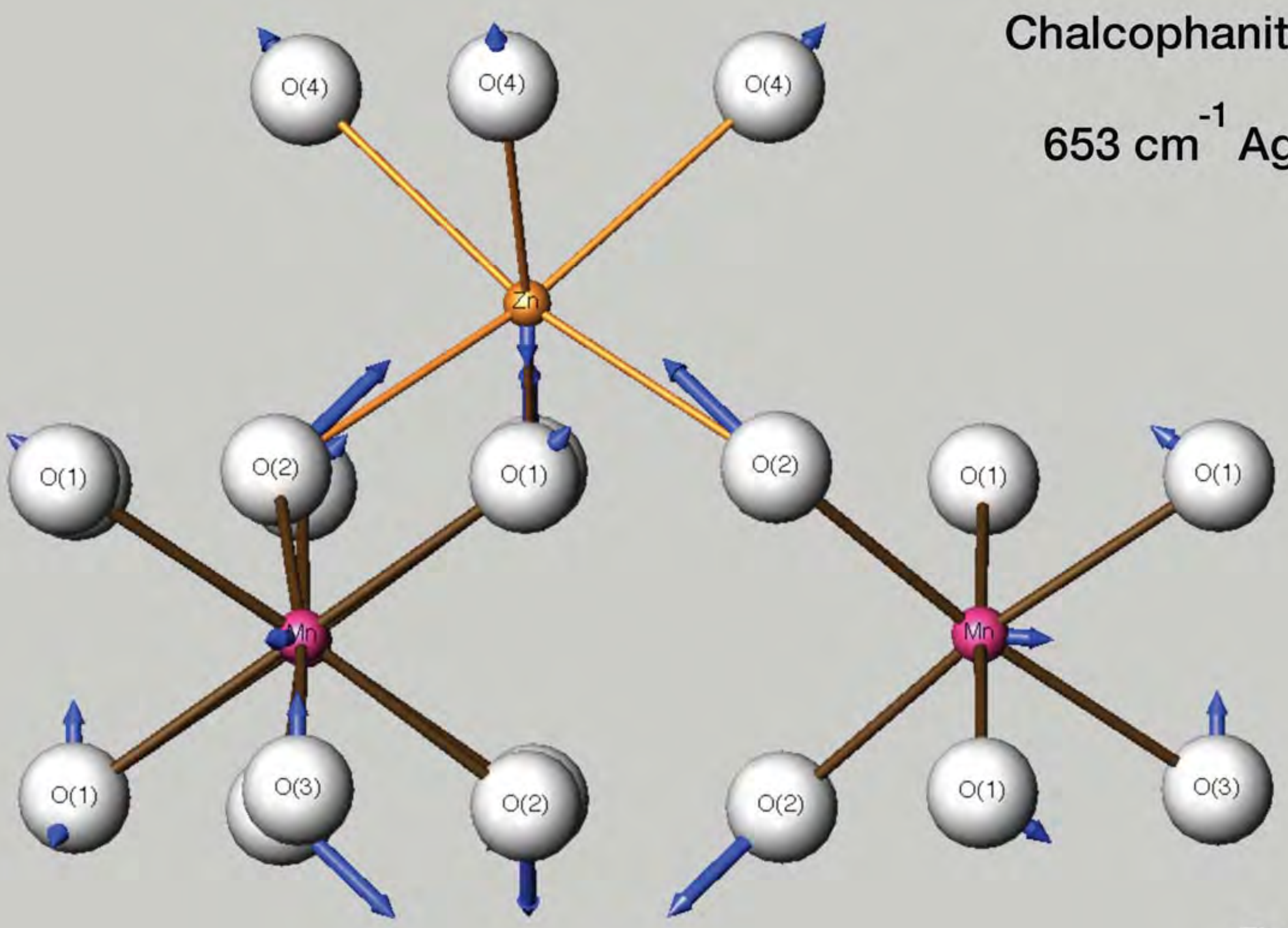

Chalcophanite

653 cm^{-1} Ag

Fig. 6b

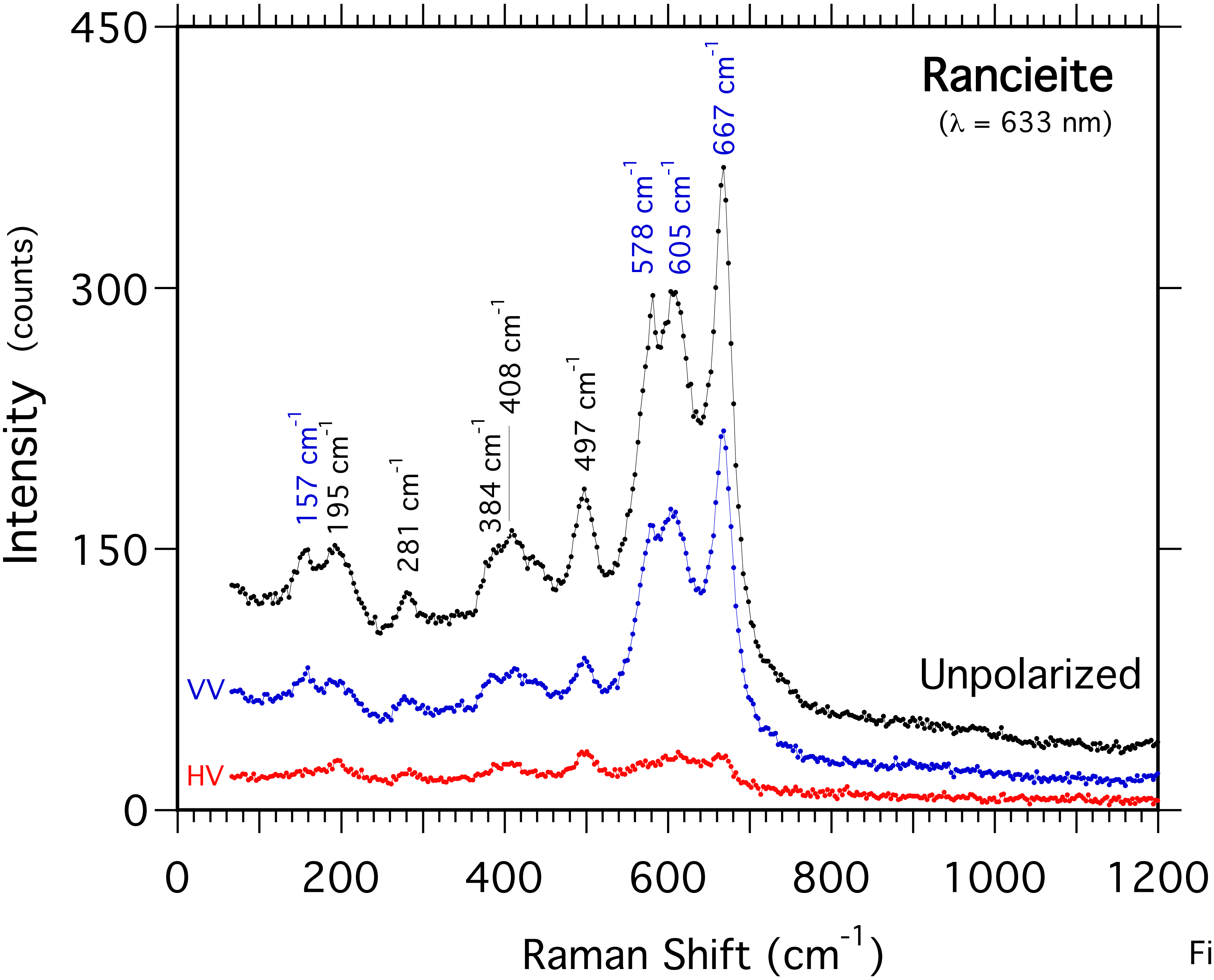
Rancieite
(λ = 633 nm)
Unpolarized
VV
HV
157 cm-1
195 cm-1
281 cm-1
384 cm-1
408 cm-1
497 cm-1
578 cm-1
605 cm-1
667 cm-1
Intensity (counts)
0
150
300
450
0
200
400
600
800
1000
1200
Raman Shift (cm-1)

Fig. 7

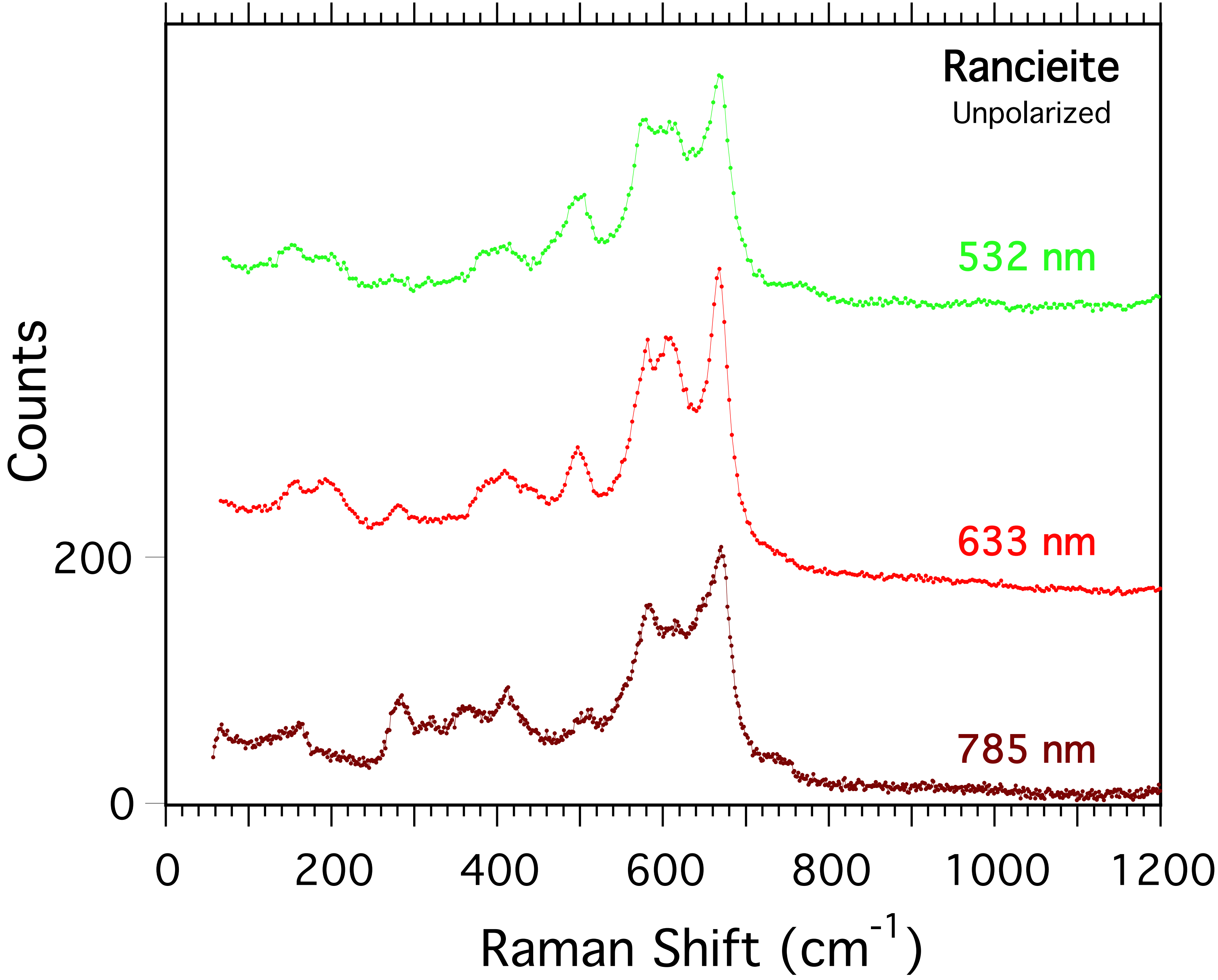
Rancieite
Unpolarized
532 nm
633 nm
785 nm
Counts
200
0
0
200
400
600
800
1000
1200
Raman Shift (cm^{-1})

Fig. 8

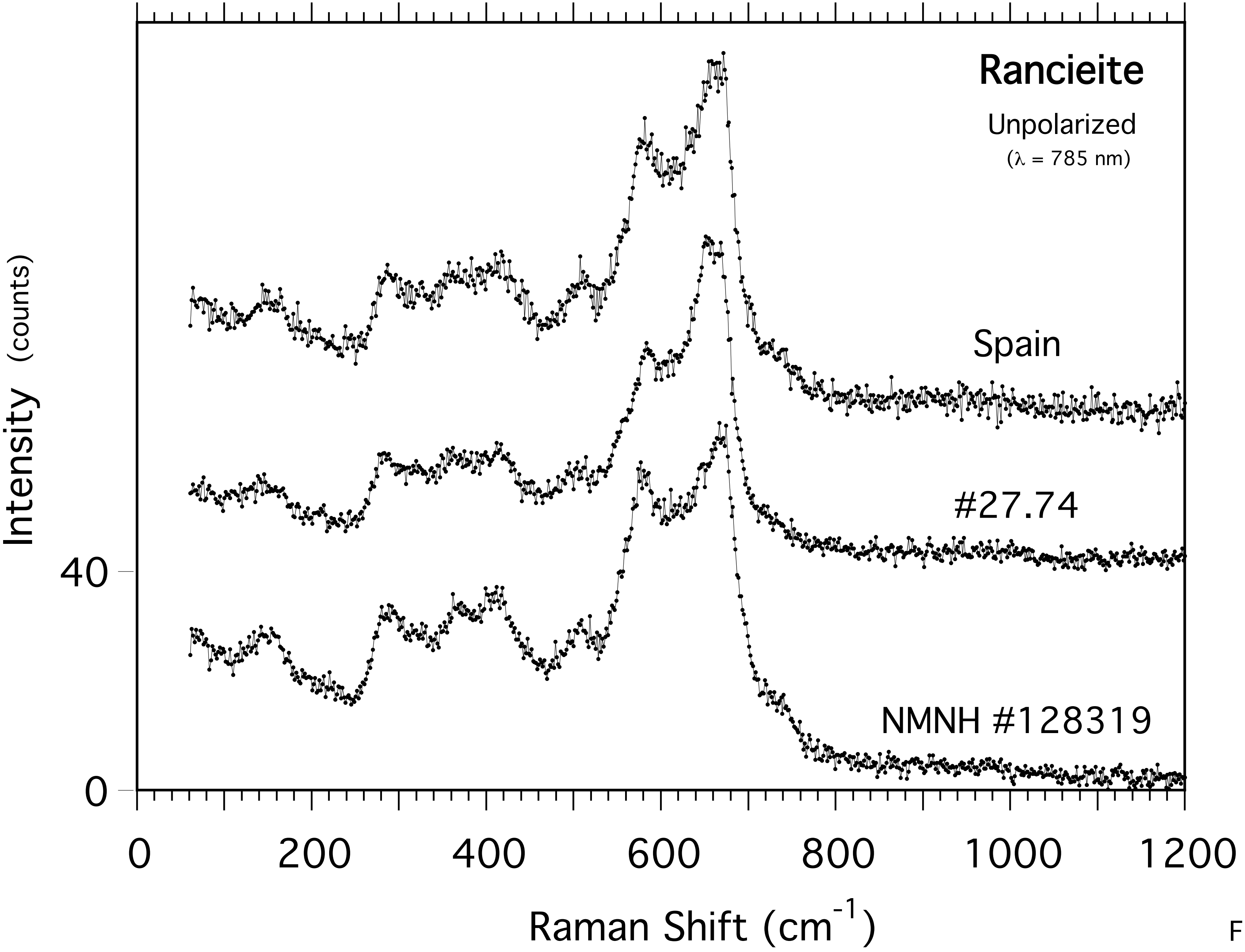

Rancieite
Unpolarized
(λ = 785 nm)
Spain
#27.74
NMNH #128319
Intensity (counts)
40
0
0
200
400
600
800
1000
1200
Raman Shift (cm^{-1})

Fig. 9

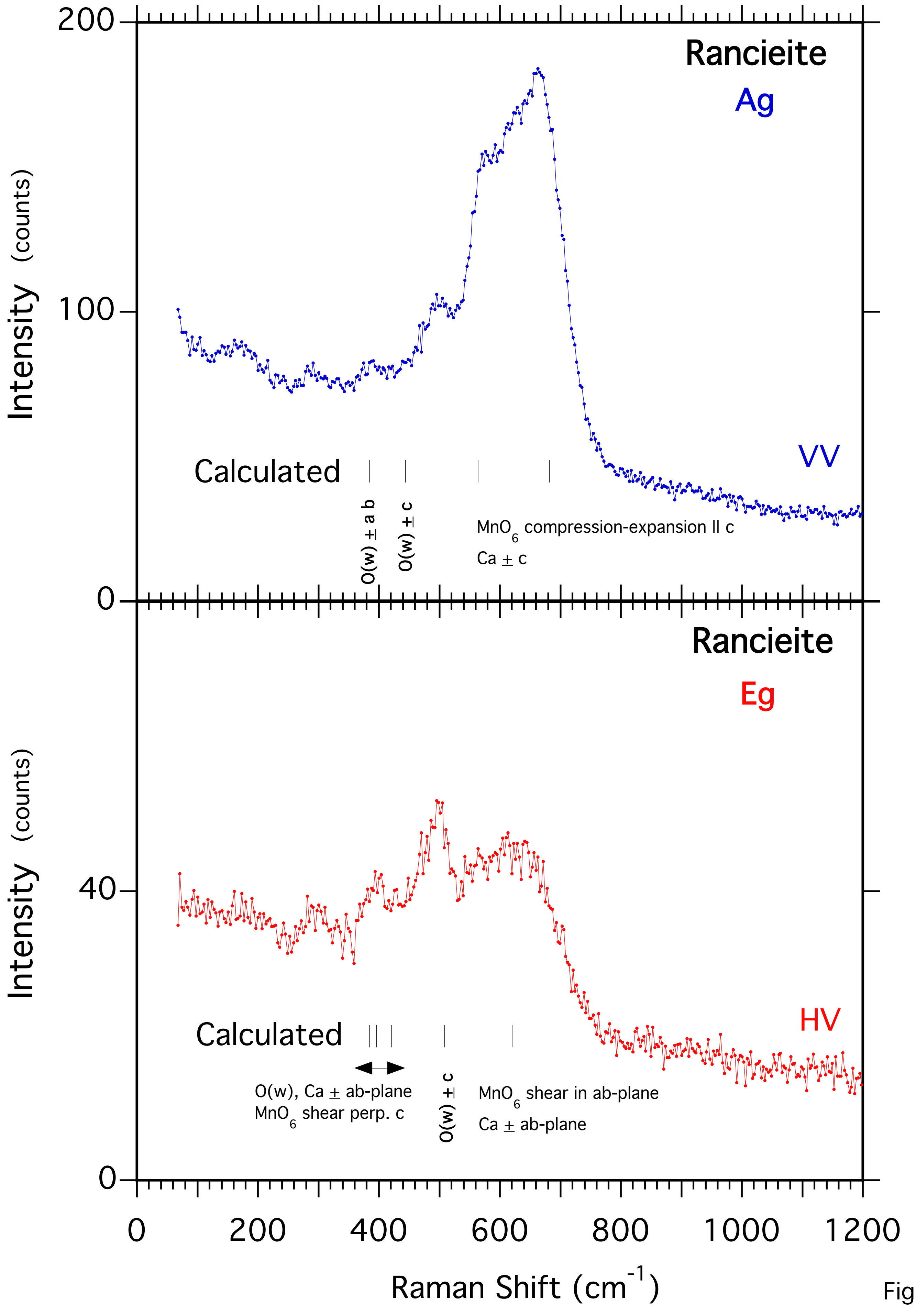
200
100
0
Intensity (counts)
Rancieite
Ag
VV
Calculated
O(w) ± a b
O(w) ± c
MnO_6 compression-expansion || c
Ca ± c
Rancieite
Eg
HV
40
0
Intensity (counts)
Calculated
O(w), Ca ± ab-plane
MnO_6 shear perp. c
O(w) ± c
MnO_6 shear in ab-plane
Ca ± ab-plane
0
200
400
600
800
1000
1200
Raman Shift (cm^{-1})

Fig. 10

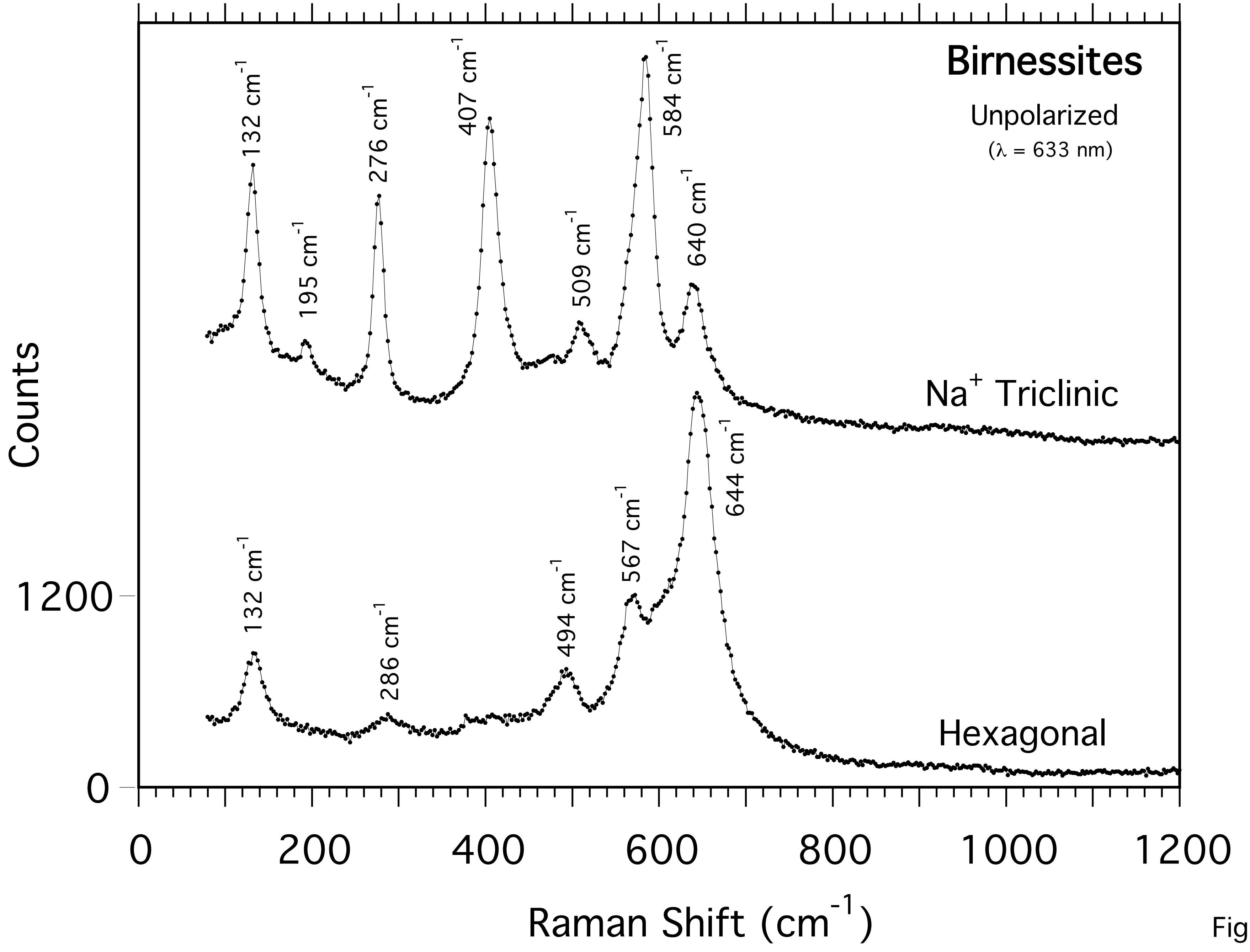
Birnessites
Unpolarized
(λ = 633 nm)
132 cm-1
195 cm-1
276 cm-1
407 cm-1
509 cm-1
584 cm-1
640 cm-1
Na+ Triclinic
132 cm-1
286 cm-1
494 cm-1
567 cm-1
644 cm-1
Hexagonal
Counts
1200
0
0
200
400
600
800
1000
1200
Raman Shift (cm-1)

Fig. 11a

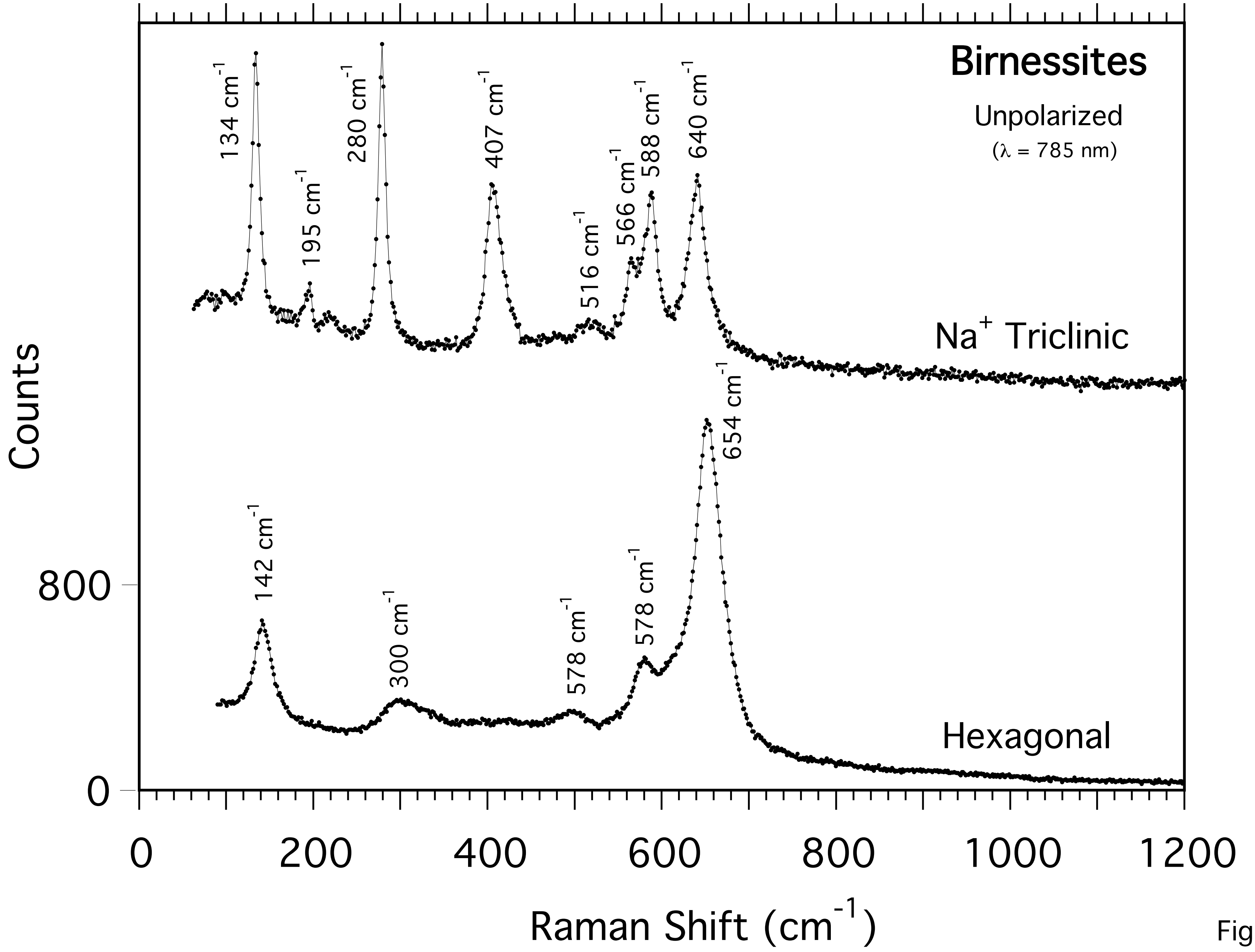
Birnessites
Unpolarized
(λ = 785 nm)
134 cm-1
195 cm-1
280 cm-1
407 cm-1
516 cm-1
566 cm-1
588 cm-1
640 cm-1
Na+ Triclinic
654 cm-1
142 cm-1
300 cm-1
578 cm-1
578 cm-1
Hexagonal
Counts
800
0
0
200
400
600
800
1000
1200
Raman Shift (cm-1)

Fig. 11b

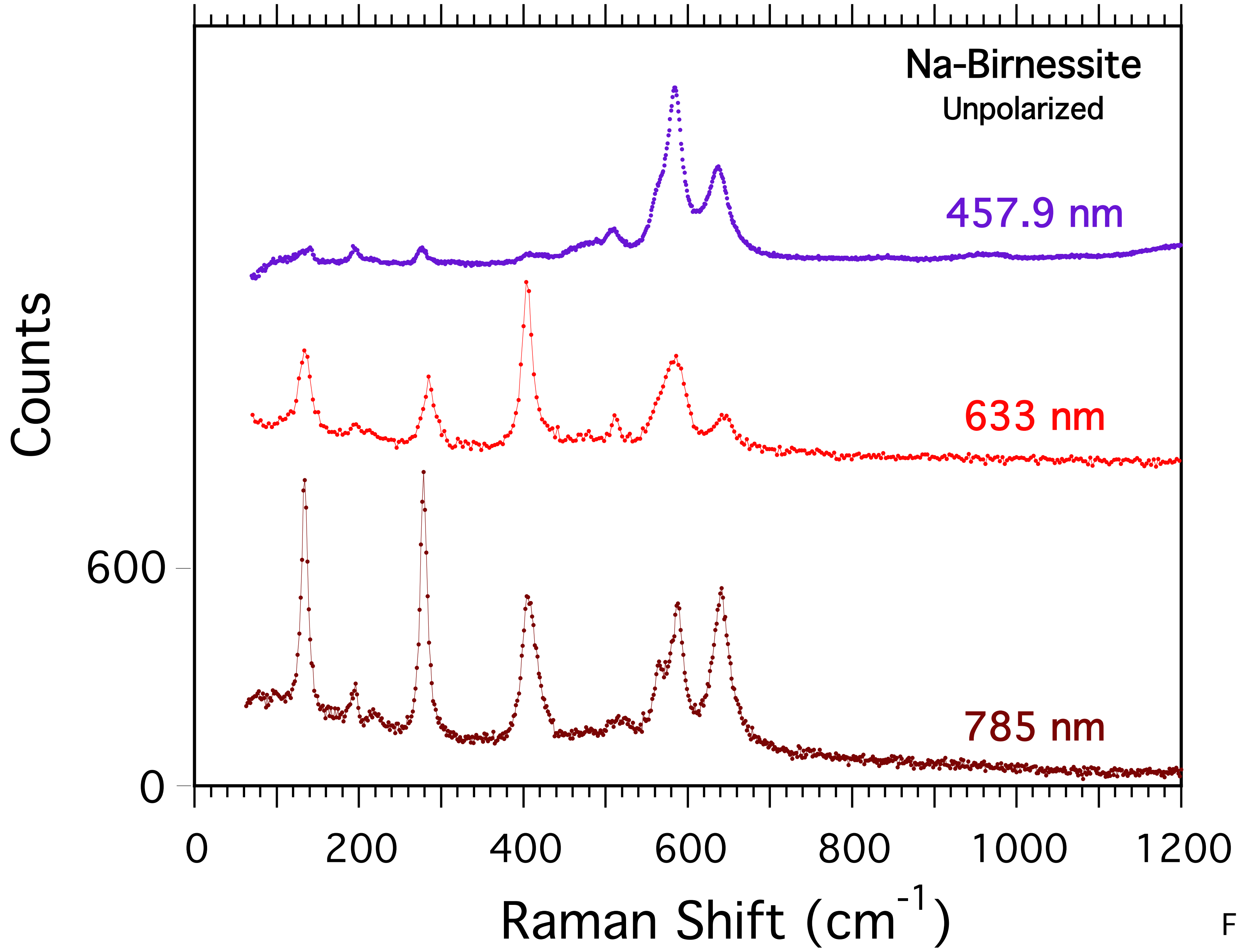
Na-Birnessite
Unpolarized
457.9 nm
633 nm
785 nm
Counts
600
0
0
200
400
600
800
1000
1200
Raman Shift (cm^{-1})

Fig. 12a

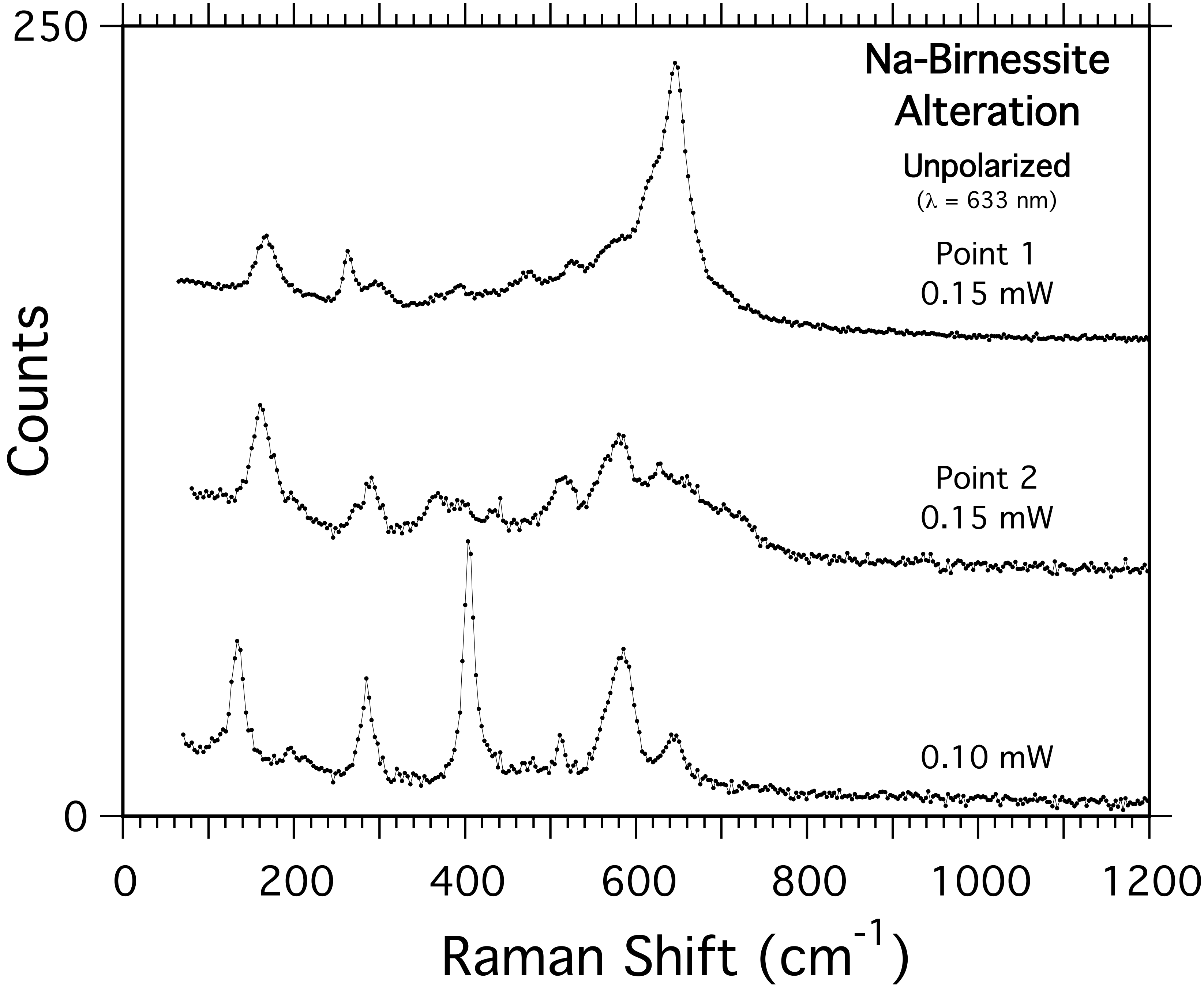

250
0
Counts
0
200
400
600
800
1000
1200
Raman Shift (cm^{-1})
Na-Birnessite
Alteration
Unpolarized
(λ = 633 nm)
Point 1
0.15 mW
Point 2
0.15 mW
0.10 mW

Fig. 12b

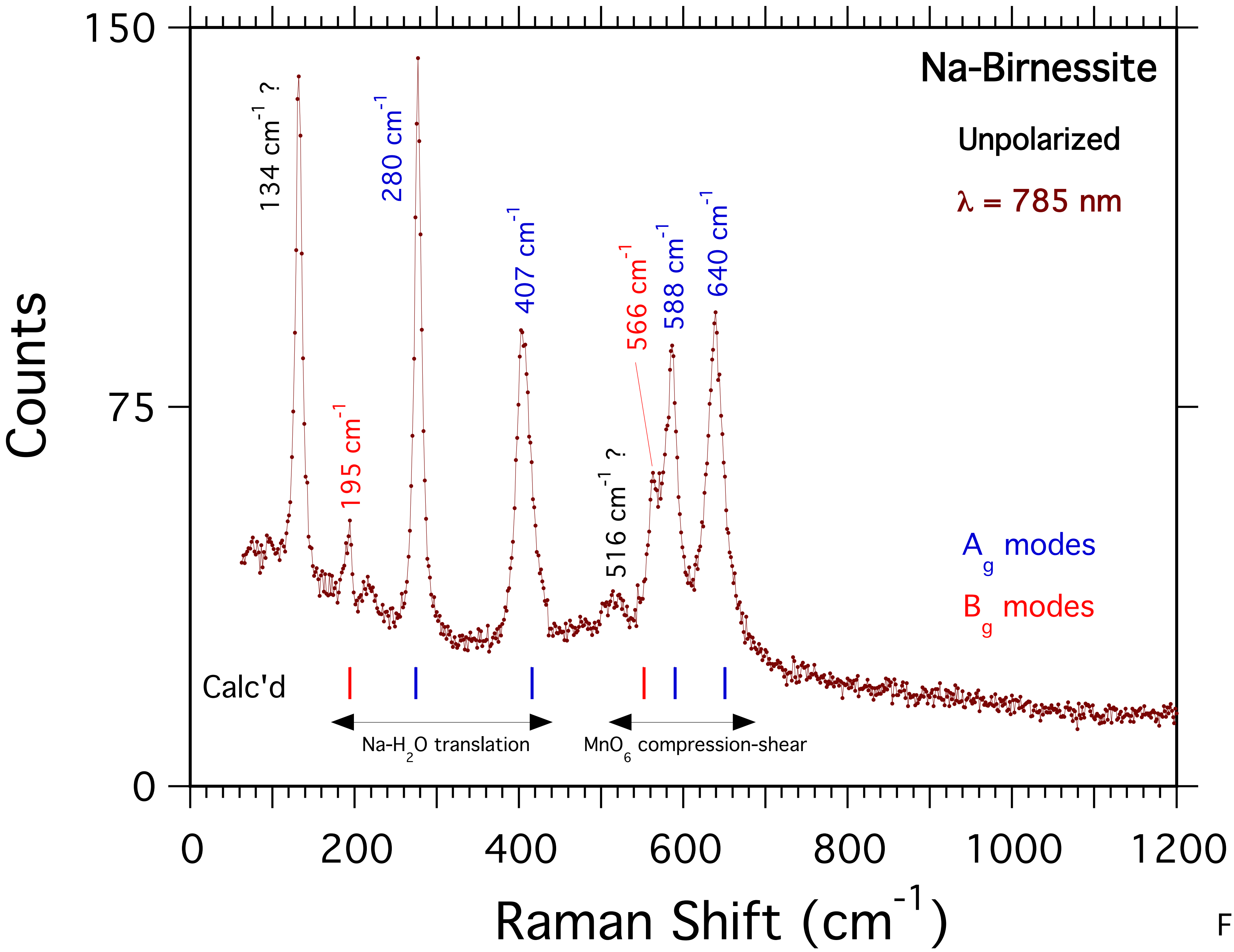

Na-Birnessite
Unpolarized
λ = 785 nm
134 cm-1 ?
195 cm-1
280 cm-1
407 cm-1
516 cm-1 ?
566 cm-1
588 cm-1
640 cm-1
Ag modes
Bg modes
Calc'd
Na-H2O translation
MnO6 compression-shear
Counts
150
75
0
0
200
400
600
800
1000
1200
Raman Shift (cm-1)

Fig. 13

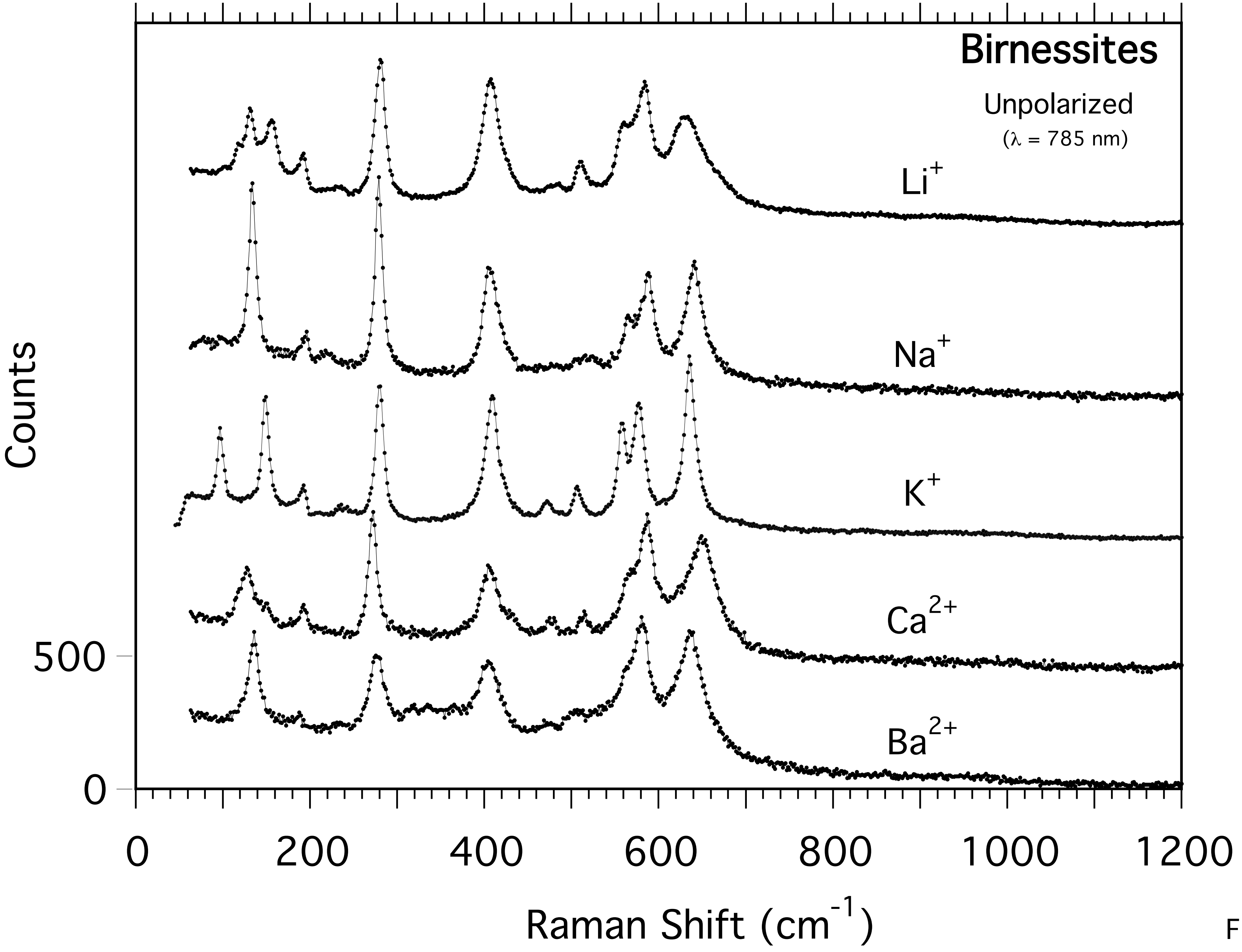
Birnessites
Unpolarized
(λ = 785 nm)
Li+
Na+
K+
Ca2+
Ba2+
Counts
500
0
0
200
400
600
800
1000
1200
Raman Shift (cm-1)

Fig. 14

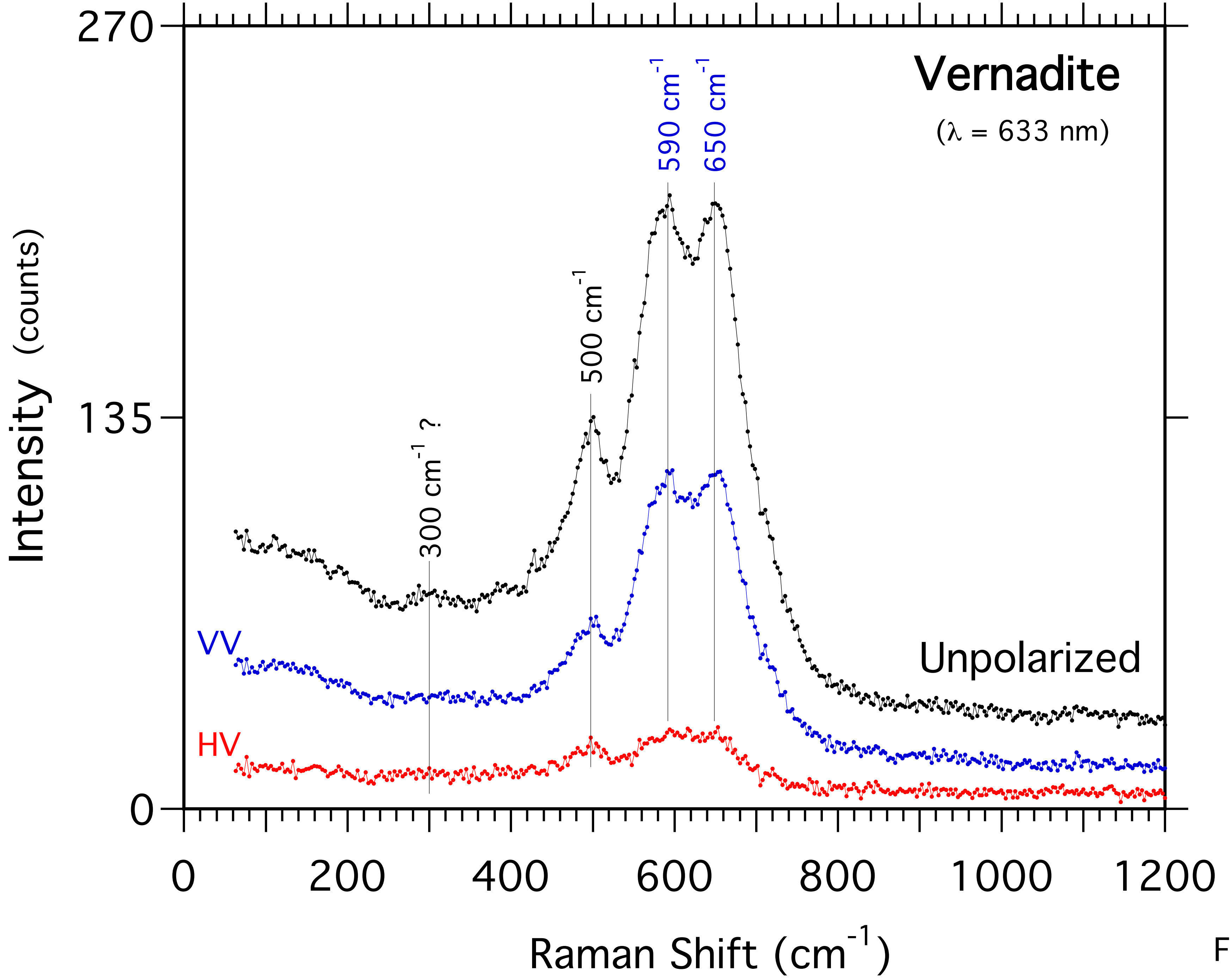
Vernadite
(λ = 633 nm)
590 cm⁻¹
650 cm⁻¹
500 cm⁻¹
300 cm⁻¹ ?
VV
HV
Unpolarized
Intensity (counts)
270
135
0
0
200
400
600
800
1000
1200
Raman Shift (cm⁻¹)

Fig. 15

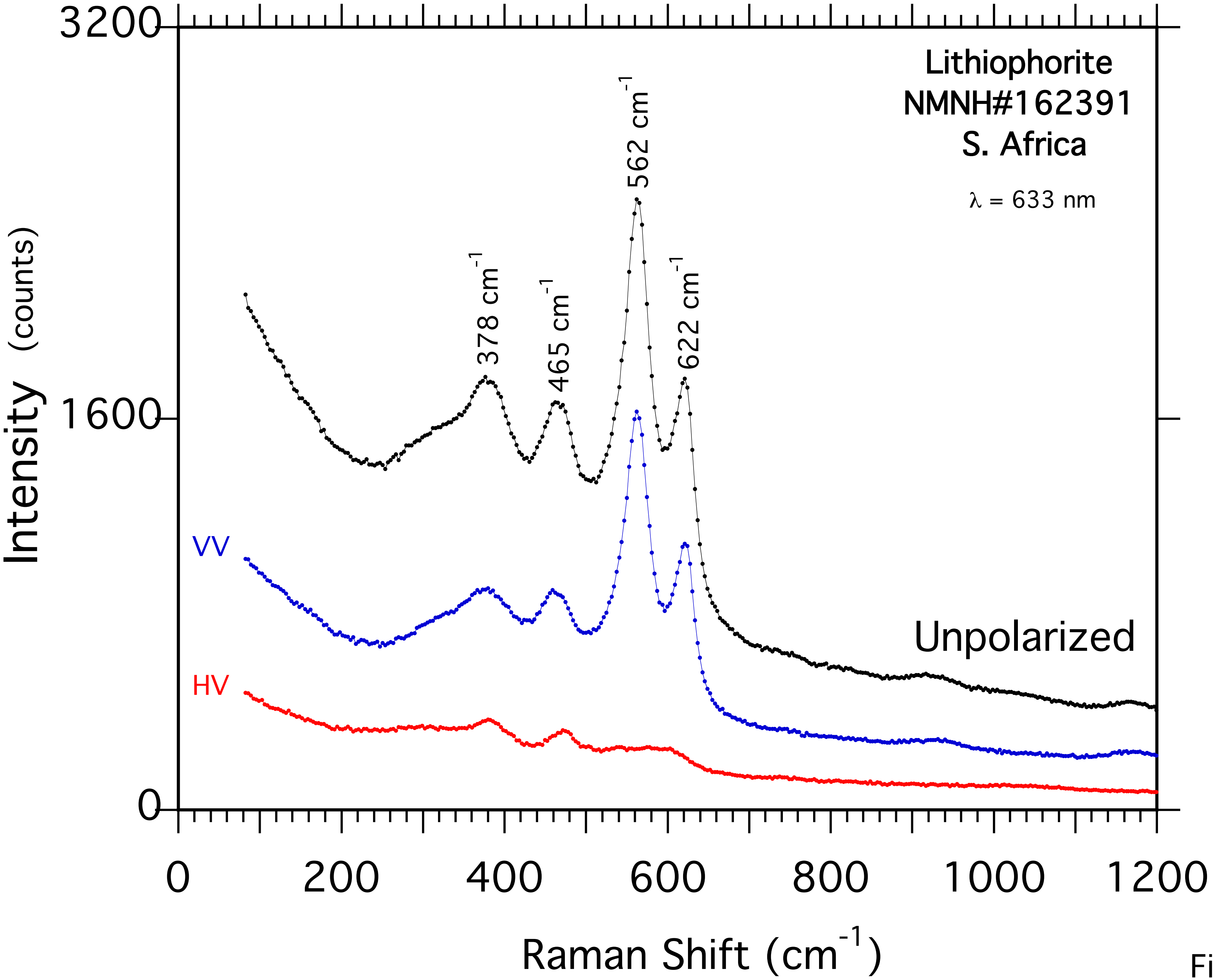
Lithiophorite
NMNH#162391
S. Africa
λ = 633 nm
378 cm^{-1}
465 cm^{-1}
562 cm^{-1}
622 cm^{-1}
VV
HV
Unpolarized
Intensity (counts)
3200
1600
0
0
200
400
600
800
1000
1200
Raman Shift (cm^{-1})

Fig. 16

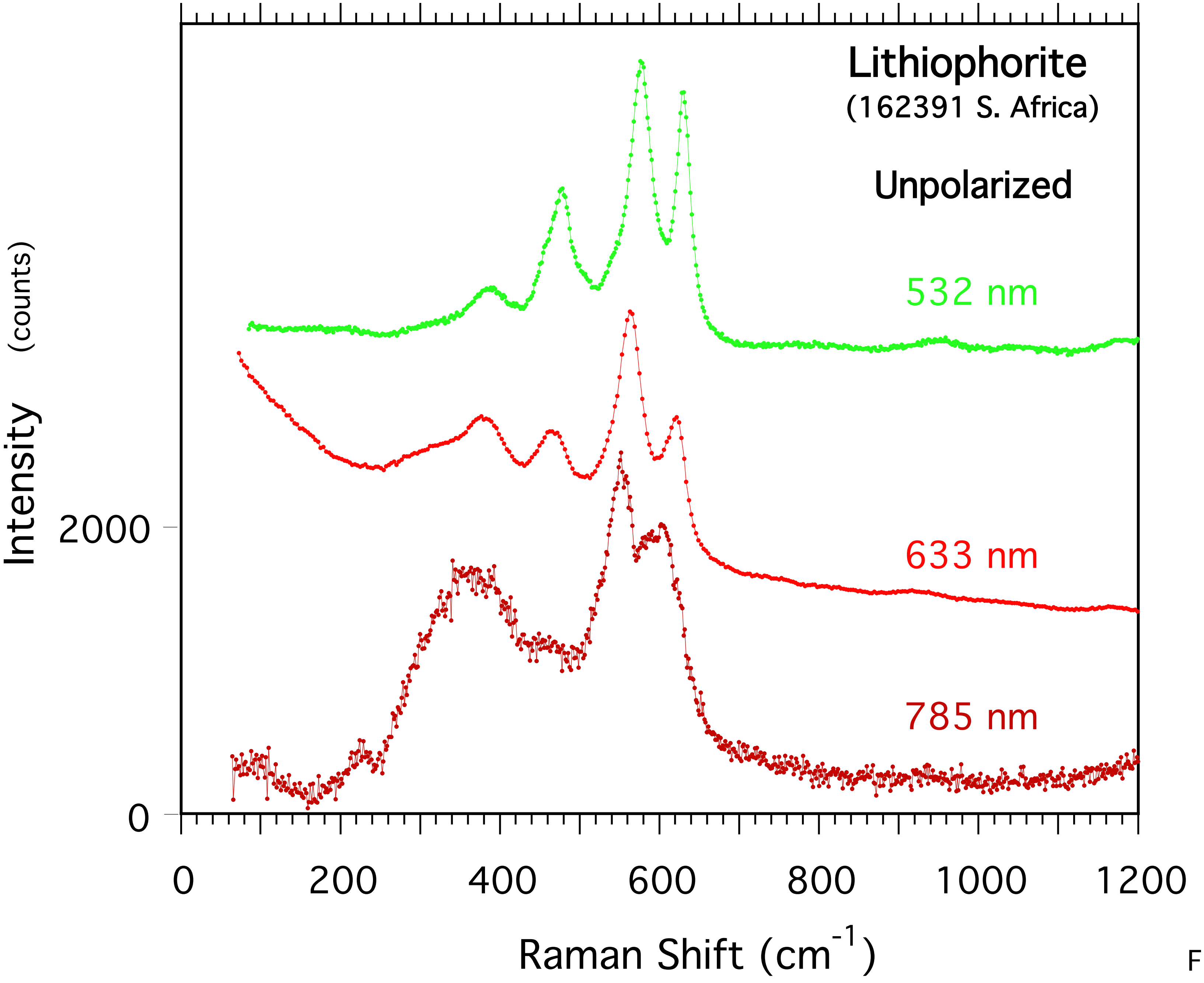
Lithiophorite
(162391 S. Africa)
Unpolarized
532 nm
633 nm
785 nm
Intensity (counts)
2000
0
0
200
400
600
800
1000
1200
Raman Shift (cm-1)

Fig. 17

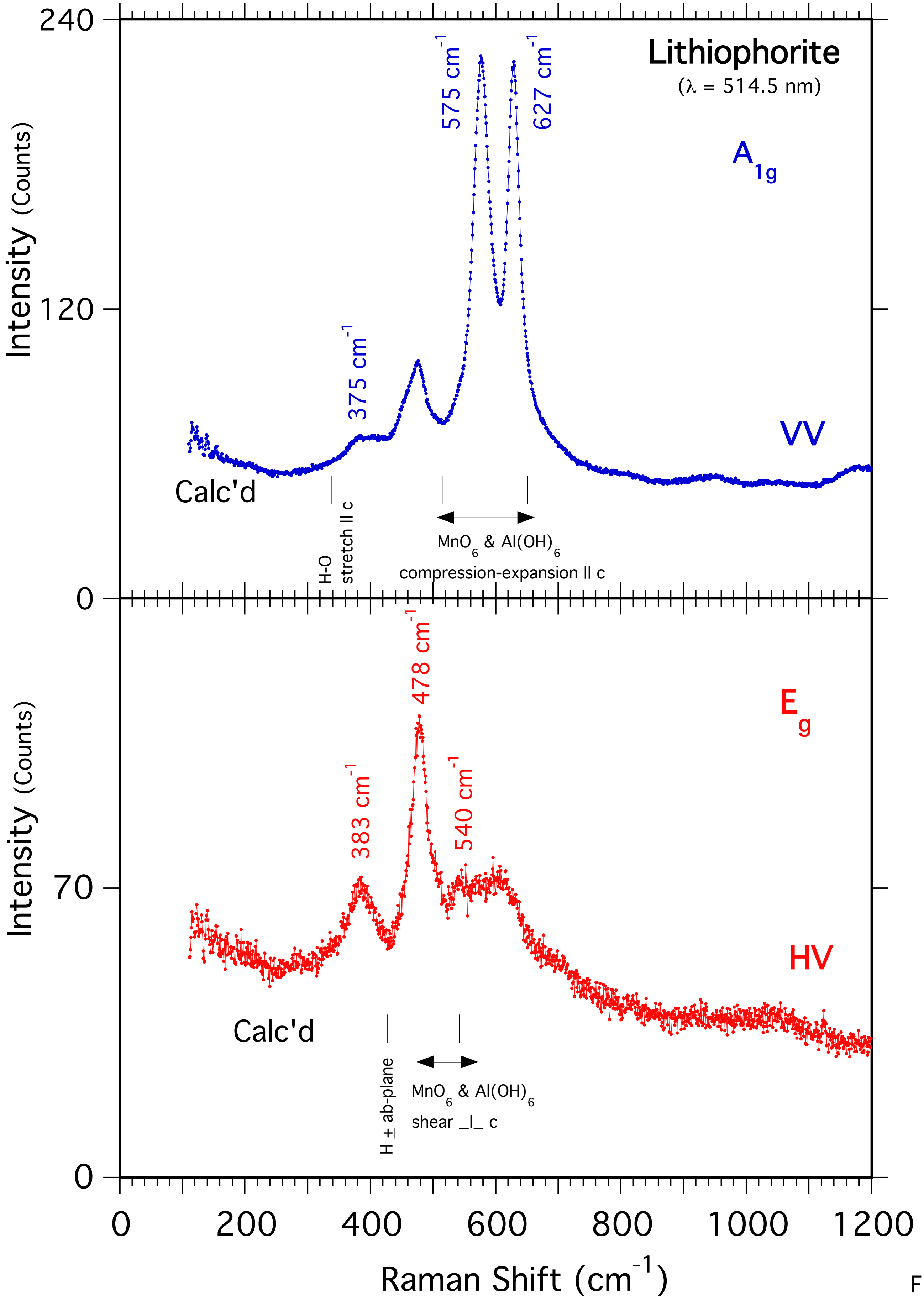
Lithiophorite
(λ = 514.5 nm)
A1g
VV
575 cm-1
627 cm-1
375 cm-1
Calc'd
H-O stretch ‖ c
MnO6 & Al(OH)6 compression-expansion ‖ c
Eg
HV
478 cm-1
383 cm-1
540 cm-1
Calc'd
H ± ab-plane
MnO6 & Al(OH)6 shear _|_ c
Intensity (Counts)
240
120
0
Intensity (Counts)
70
0
0
200
400
600
800
1000
1200
Raman Shift (cm-1)

Fig. 18

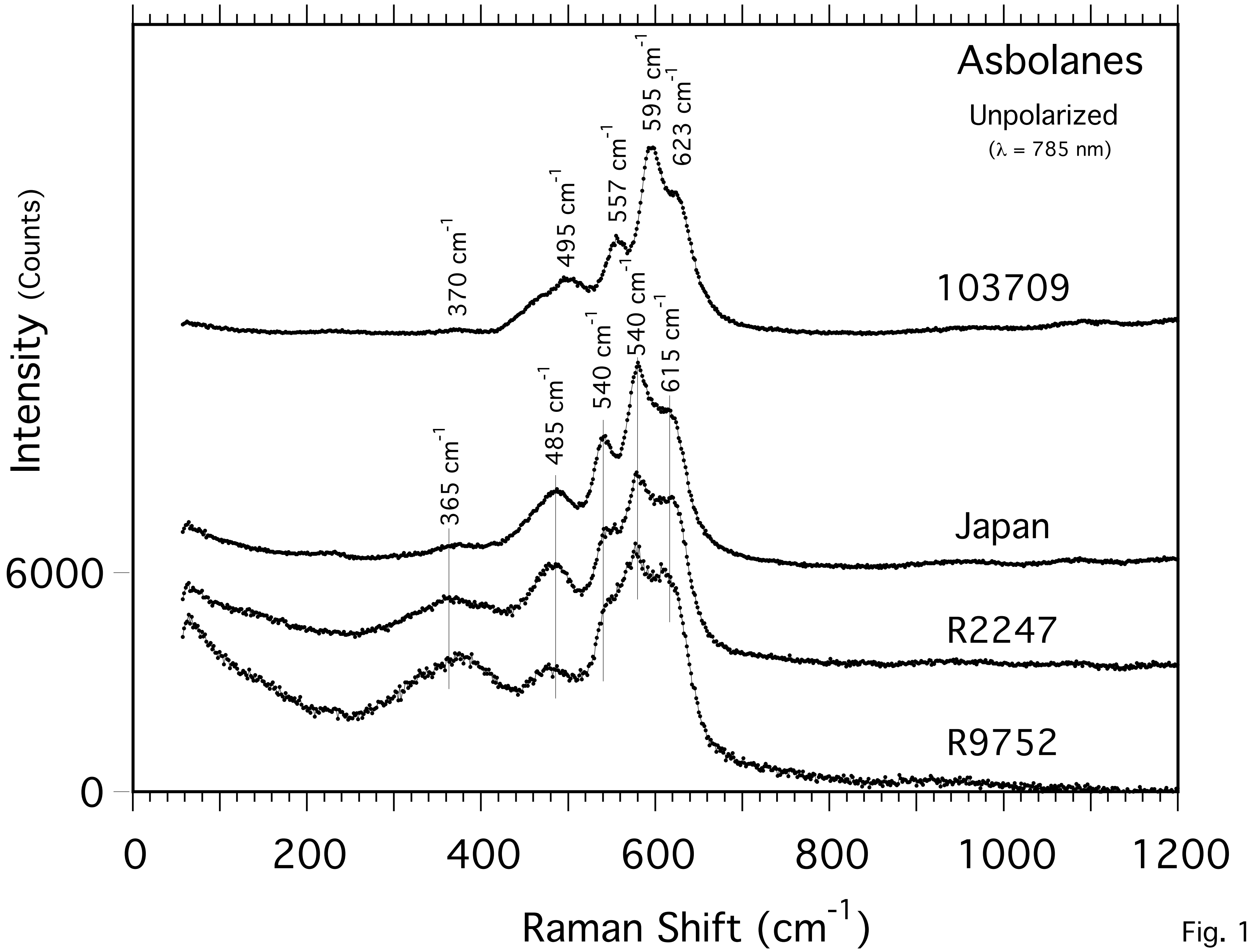
Asbolanes
Unpolarized
(λ = 785 nm)
370 cm-1
495 cm-1
557 cm-1
595 cm-1
623 cm-1
103709
365 cm-1
485 cm-1
540 cm-1
540 cm-1
615 cm-1
Japan
R2247
R9752
Intensity (Counts)
6000
0
0
200
400
600
800
1000
1200
Raman Shift (cm-1)

Fig. 19

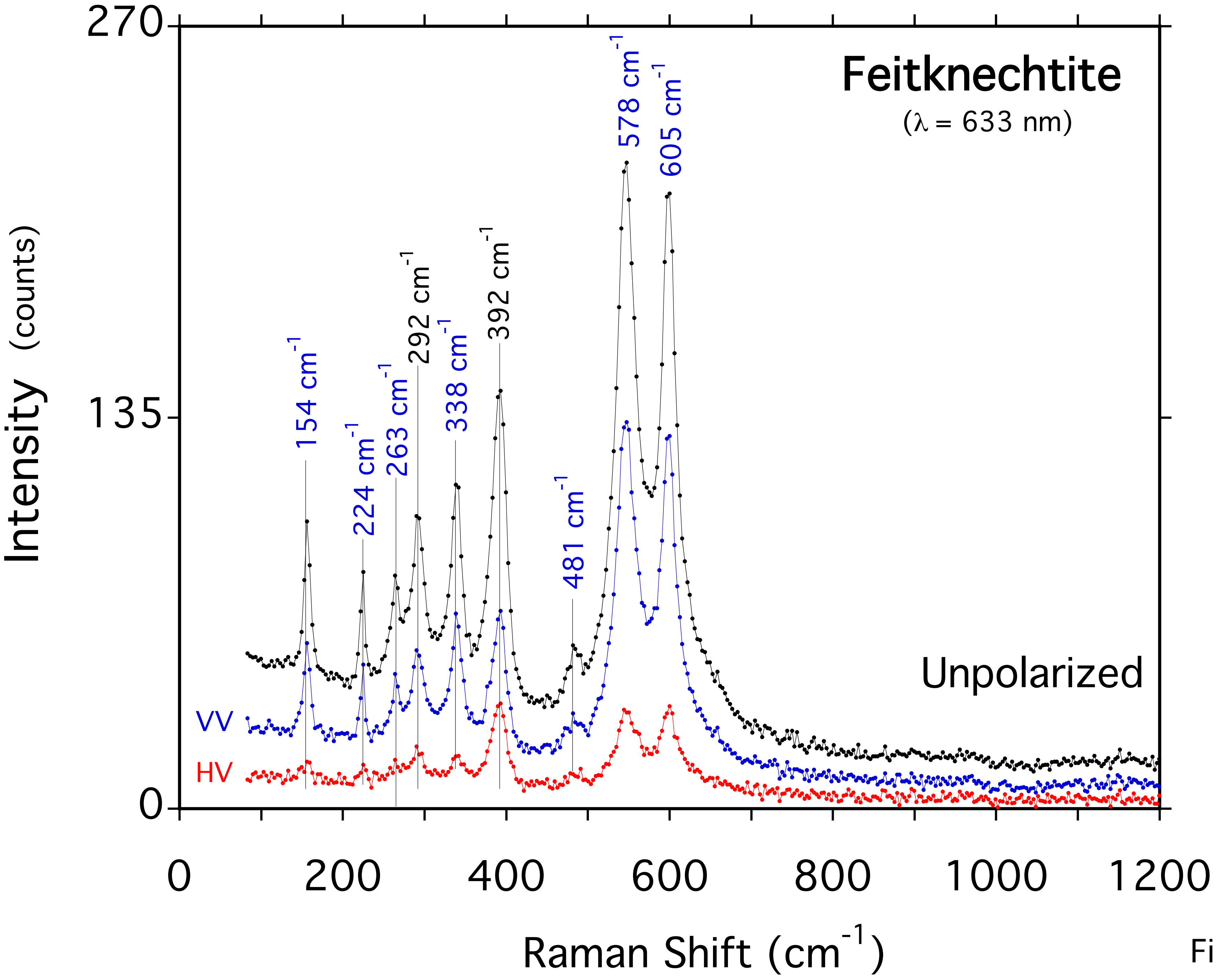
Feitknechtite
(λ = 633 nm)
Unpolarized
VV
HV
154 cm-1
224 cm-1
263 cm-1
292 cm-1
338 cm-1
392 cm-1
481 cm-1
578 cm-1
605 cm-1
Intensity (counts)
270
135
0
0
200
400
600
800
1000
1200
Raman Shift (cm-1)

Fig. 20

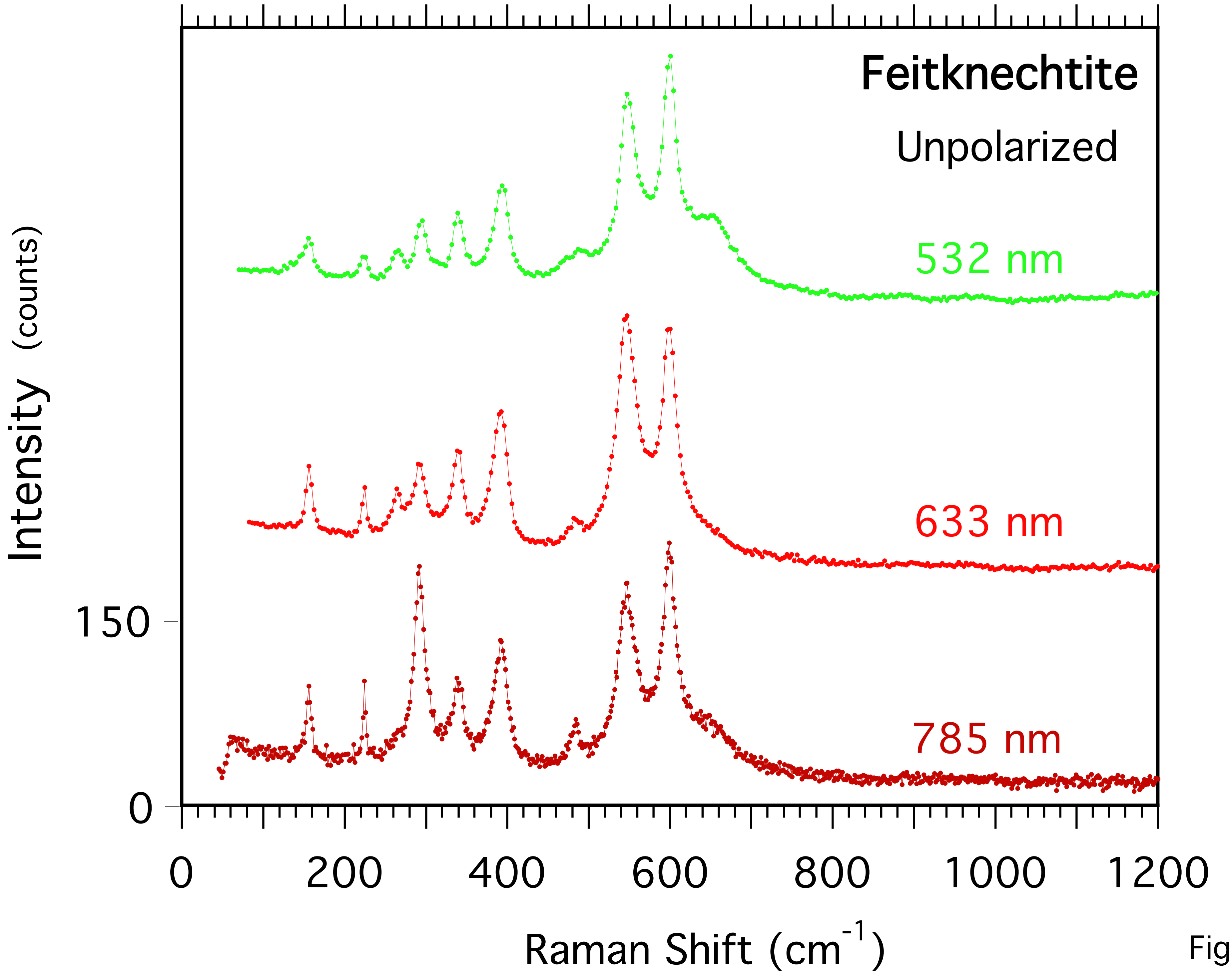
Feitknechtite
Unpolarized
532 nm
633 nm
785 nm
Intensity (counts)
150
0
0
200
400
600
800
1000
1200
Raman Shift (cm^{-1})

Fig. 21

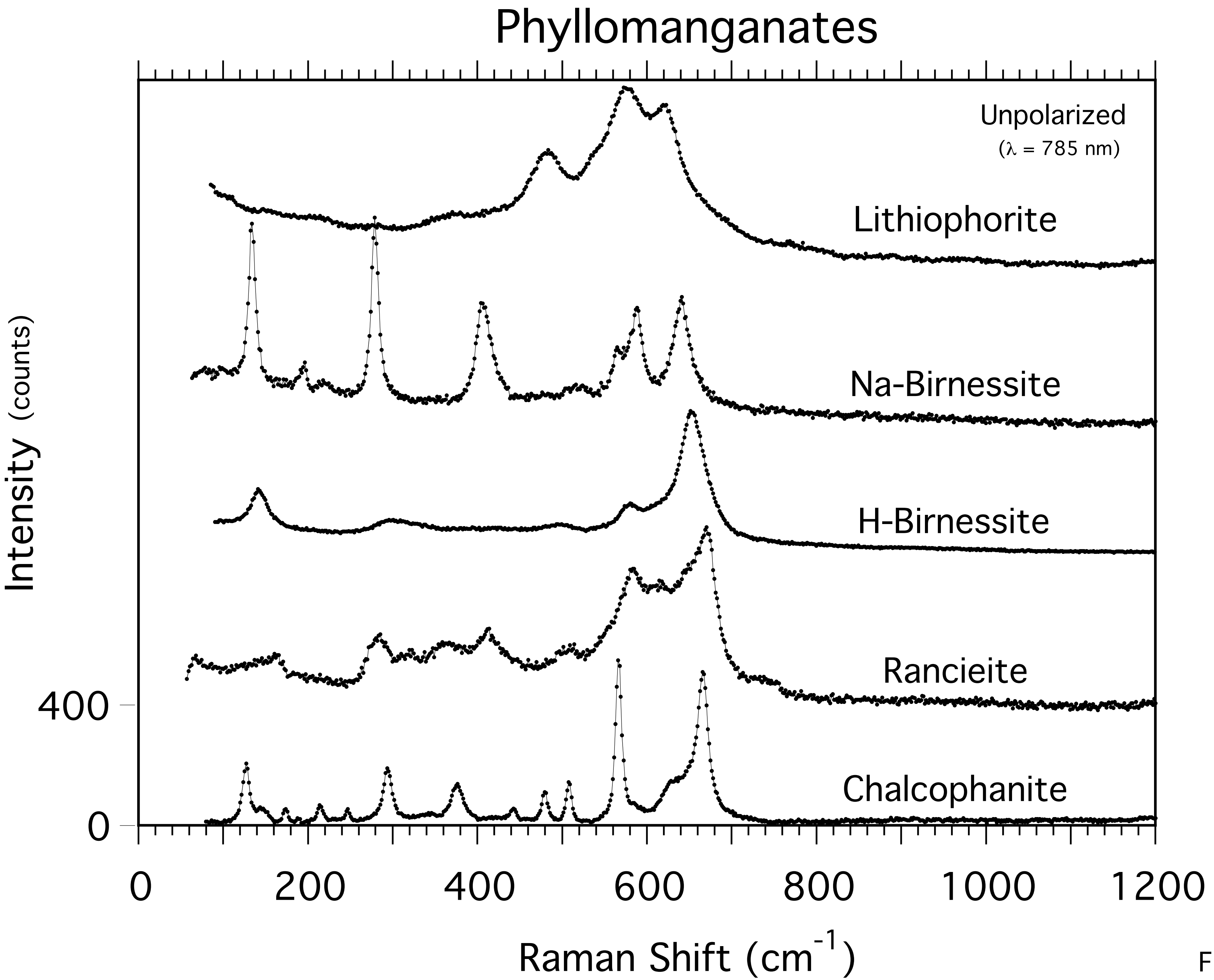
Phyllomanganates
Unpolarized
(λ = 785 nm)
Lithiophorite
Na-Birnessite
H-Birnessite
Rancieite
Chalcophanite
Intensity (counts)
400
0
0
200
400
600
800
1000
1200
Raman Shift (cm-1)

Fig. 22

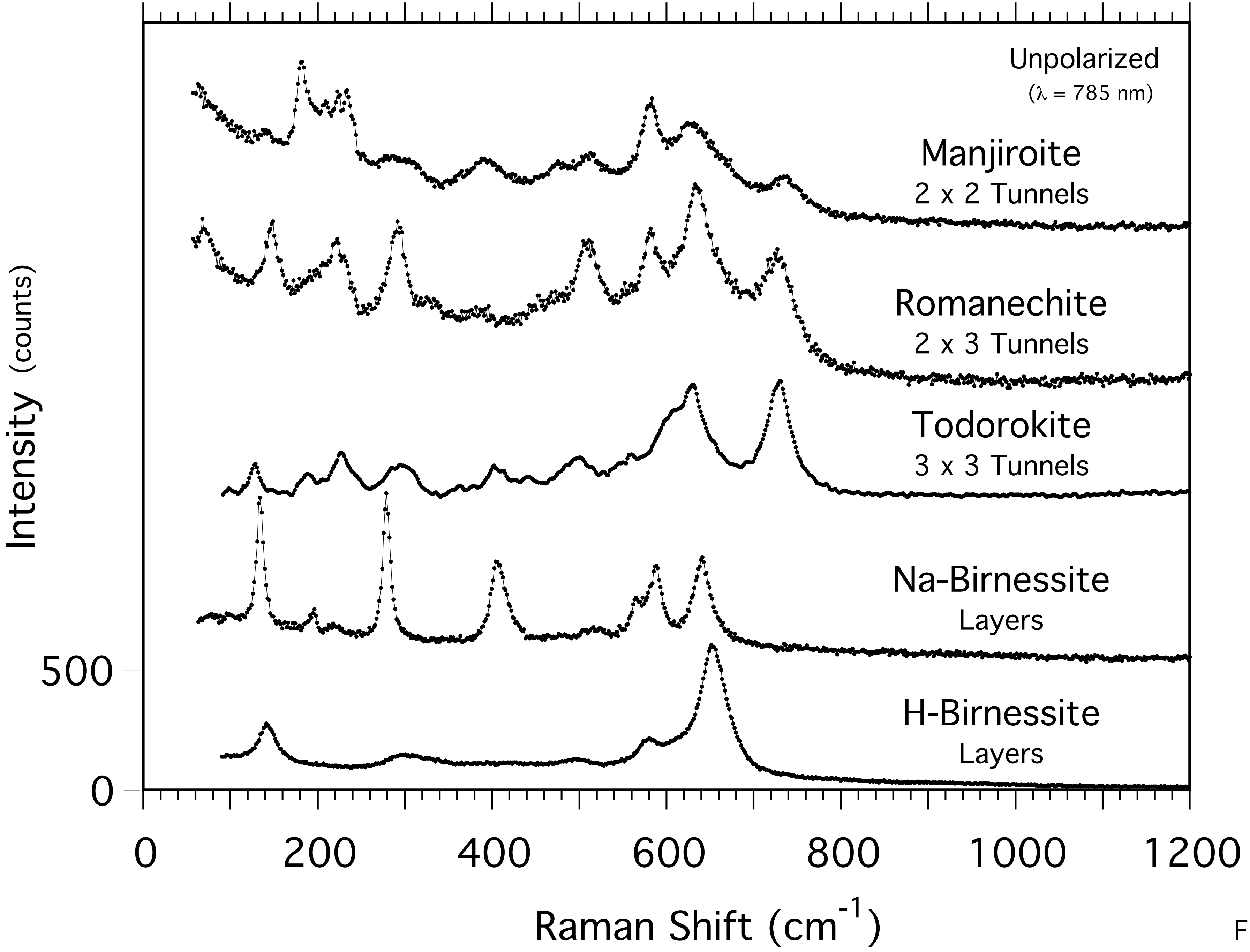
Unpolarized
(λ = 785 nm)
Manjiroite
2 x 2 Tunnels
Romanechite
2 x 3 Tunnels
Todorokite
3 x 3 Tunnels
Na-Birnessite
Layers
H-Birnessite
Layers
Intensity (counts)
500
0
0
200
400
600
800
1000
1200
Raman Shift (cm-1)

Fig. 23

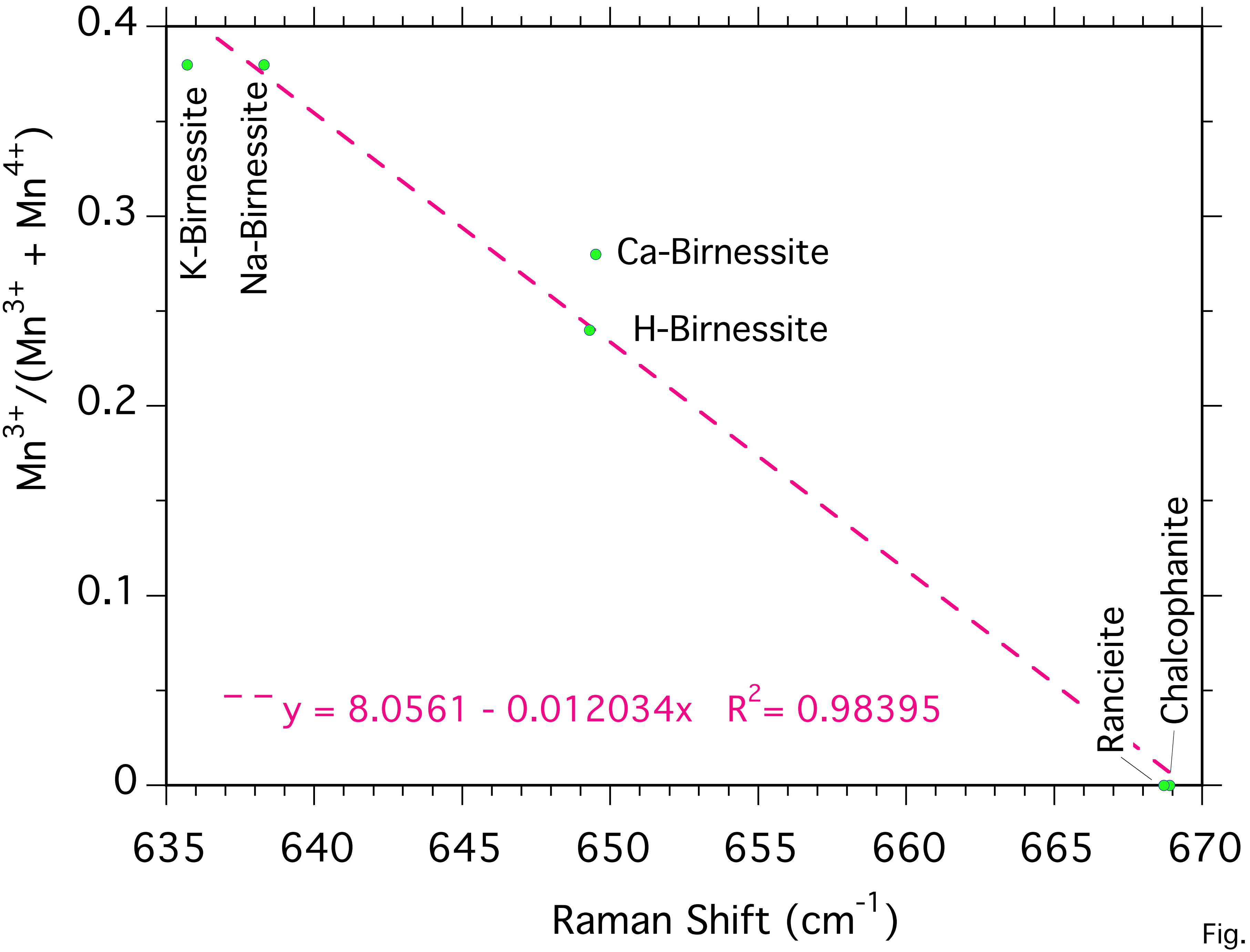
0.4
0.3
0.2
0.1
0
635
640
645
650
655
660
665
670
Raman Shift (cm^{-1})
Mn^{3+}/(Mn^{3+} + Mn^{4+})
K-Birnessite
Na-Birnessite
Ca-Birnessite
H-Birnessite
Rancieite
Chalcophanite
y = 8.0561 - 0.012034x R^2= 0.98395

Fig. 24

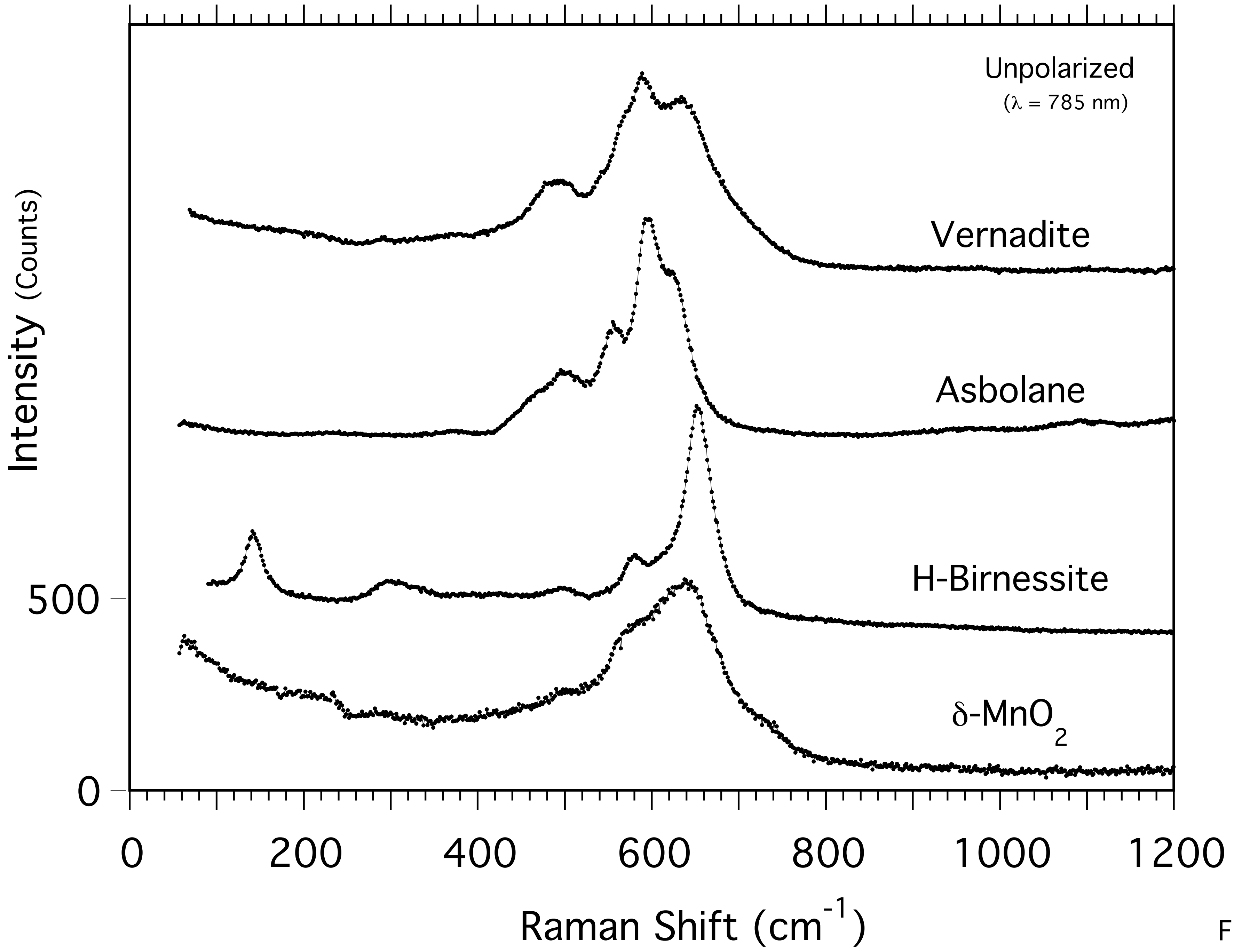
Unpolarized
(λ = 785 nm)
Vernadite
Asbolane
H-Birnessite
δ-MnO$_2$
Intensity (Counts)
500
0
0
200
400
600
800
1000
1200
Raman Shift (cm^{-1})

Fig. 25